Università degli Studi di Napoli "Federico II"

PhD. Dissertation

Design Concepts and Simulation Strategies of Integrated Optical Devices

Martina De Laurentis

a.a 2006-2007

A Jacopo

Contents

Acknowledgements

Prima di ogni altro ringrazio il professor Breglio che mi ha dato la possibilità di svolgere questo lavoro accogliendomi nel suo gruppo; ringrazio il professor Irace le cui idee mi hanno guidato e illuminato durante il lavoro; ringrazio entrambi per la disponibilità e la grande umanità dimostrata nei momenti di bisogno.

Ringrazio poi Lucio, il mio carissimo compagno di avventura in questi tre anni di studi, perché pazientemente mi ha sopportata.

Ringrazio Michele, che ha portato la sua allegria nel nostro laboratorio e il suo entusiasmo.

Ringrazio Alessia, con la quale abbiamo diviso tante piccole esperienze nel corso di questi studi.

Ringrazio con tutta l'anima i miei carissimi genitori, che mi hanno sempre sostenuta, specialmente per il loro aiuto in quest'ultimo anno di 'nuova organizzazione'.

Ringrazio mia sorella perché mi ha sempre spronata ad andare avanti.

Ringrazio la mia carissma amica Antonella, per il bene che mi vuole nonostnte i miei mille difetti.

Infine, non per ultimi, ringrazio Pasquale ed il mio piccolino, Jacopo. Il primo perché mi sa amare come nessun altro saprebbe fare e perché sopporta la mie scarse doti domestiche; il secondo perché da quando esiste ha illuminato di una luce nuova la mia anima e le mie giornate.

Chapter 1

Introduction

The semiconductor optoelectronic devices in the last years are capturing an increasing relevant role in the communication and computational scenery thanks to their high performance in terms of speed and processing efficiency (computing), transmission, and reception of information. Parallely it is increasing the necessity to have efficient tools to model and to simulate their behaviors in order to allow the best design.

An optoelectronic device, as the name suggests, is a device in which the electronic features of the materials are coupled with the optics ones to allow the driving of optical signals by means of electric signals. An integrated optoelectronic device is a device built on the same substrate of the electrical circuitry.

Nowadays a large number of optical modulators, filters and other functions which are considerable for telecommunication networks have been proposed [1, 2, 3, 4, 5, 6, 7] as integrated or embedded in dielectric rib/ridge waveguides. Many of them share the common feature of being based on the propagation of the light beam inside a waveguide, designed to sustain only its fundamental mode of propagation to allow lower insertion losses when coupled to optical fibers.

Nevertheless at begin of my work as integrated optoelectronic designer, I came against a problem which could seems simple and a solved question. It concerns the definition of the single-mode condition of this widely used basic element of the integrated optoelectronic devices: the rib waveguide. In fact, as observed in [8], most of authors in the past assumed *a priori* that a single-mode rib waveguide must have the same transverse dimensions as a single-mode slab waveguide, since a rib waveguide is a slab waveguide

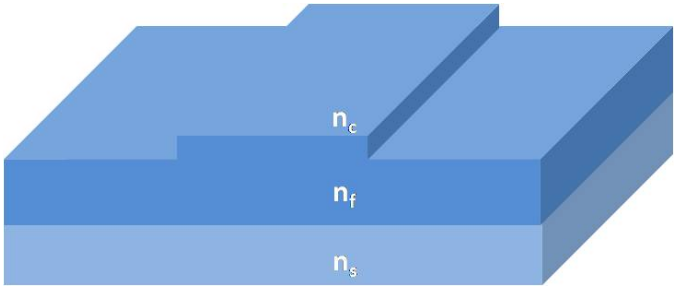

Figure 1.1: Rib waveguide.

with a ribbed region at the center. They attributed their supposition to the *Effective Index Method* (EIM), which is the common and more general method to study the 2D waveguide. From this supposition they deduce that the rib width would be smaller then the wavelength of the propagating light. Actually, rib waveguides with large cross section (that is, with lateral dimension and height much greater than the optical wavelength) were usually already employed, obtaining an excellent matching with the single mode optical fibers. Consequently the issue of establishing a single mode condition for this waveguide arose.

Since 1976, several studies have been presented in literature, but only in 1991 Richard A. Soref, Joachim Schmidtchen and Petermann himself [9] on the basis of the previous Effective Index/Mode Matching analysis performed by Petermann [10], gave a formula to establish a single mode condition. They tested the formula performing an Beam Propagation Analysis and, in the same year, realizing and observing a large cross section rib waveguide [11], designed by means of their formula.

This formula was considered the right and unequivocal condition for the designer for several years. Nevertheless Pogossian, Vescan and Vosonovici [8], based on the Rickman's experimental data [12] (it is worth to note that the available experimental data are very few), modified the Soref's formula with an corrective factor.

In the subsequent years the interest about the question is considerable increased. I have found in literature several papers [13, 14, 15, 16] (to cite only someone), which with different methods, semi-analytic, like EIM, Mode Matching or numerical, like Beam Propagation based method, confute or agree either with Soref or with Pogossian or propose correction and new

formulas. So that, at the begin of my work, it seemed that there was not an univocal and unambiguous manner to establish if a large cross-section rib waveguide can operate on single mode, but that the condition had a strong dependence on the geometry and the structure. This lead me to deduce that the first question to solve, to design optoelectronic devices, was to understand which criterion has to be followed to establish the single mode condition for a large cross-section rib waveguide, or rather to found a robust an unambiguously criterion.

During my subsequent study I found a new, robust criterion, based on an Finite Element analysis [17], by comparison between the numerical solutions found with Neumann boundary conditions and Dirichlet boundaries conditions applied when solving the eigenvalues problem.

Once assured an unambiguous criterion to establish the single mode condition of the rib waveguide, I followed the increasing request to develop an efficient and comprehensive simulation capability for optical devices.

In fact the optoelectronic devices demand the development of accurate and computationally efficient microscopic models of the physical processes that play important roles in determining optoelectronic device performance. These processes involve carrier-carrier and carrier-phonon scattering, plasma heating, carrier capture by and escape from quantum wells, and other many-body interaction processes.

The usual, old procedure was to simulate the electronic and thermal processes solving the Poisson's equation, both carrier continuity and carrier energy balance equation, the lattice heat flux equation coupled and decoupled by means of multi-dimensional general-purpose device simulators. Then to solve the scalar wave equations for the waveguides (that are the most popular basic elements of the optoelectronic integrated devices) and use numerical or semi-numerical methods to study the light propagation inside the device to predict the optical response.

In this way the source of errors due to the need of interpolating the results obtained from the electronic simulator to the second one, can be critical to predict the very small change of the physical quantity that take place in the optical processes, like the change in the refractive index.

Today different semiconductor materials based devices simulators are available for electronic modelling from both academic institutions and commercial vendors. The most popular for the electronic devices are DESSIS

[18], Taurus-Medici [19], ATLAS [20] and Minimos-NT [21], based on the Finite Elements methods (FE). These simulators contain a comprehensive and state of the art set of physical models that can be applied to all relevant semiconductor devices and operation conditions. They are capable to perform transient and AC-small signal analysis, and mixed-mode simulations that incorporate physical devices and compact models in a circuit. They are well consolidate and with a tested reliability, and, even if some of them, in the last years offered specific module for optical simulation, especially for active device simulation, like Vertical Cavity Lasers [22], generally they must be coupled with general purpose simulators to simulate the optical behavior.

So that in the last years it is increasing the interest to develop an efficient and comprehensive simulation capability for optical devices (both active and passive) including optical, electronic, and thermal processes in a self-consistent fashion, i.e. to integrate an optical package with electronics package to form a self-consistent tool for the optoelectronic integrated circuits. To this purpose, in the last decade excellent optical simulators have been developed (for example the Crosslight products, LASTIP, to simulate the operation of semiconductor laser, and PICS3D, a state of the art 3D simulator for laser diodes and related photonic devices [23]), which thus provide the electric analysis too.

On this wake, taking the advantage of the available resources, I resort to and improve an in-house code [3], based on a suitable simulation strategy which integrates the capabilities of two of the most popular and consolidate Finite Element simulators, one of electronic devices, as Silvaco/ATLAS, the other a general purpose FE solver, as Comsol Multiphysics, by means of the maybe most powerful and interactive environment in the computational scenery, MATLAB®. The code allows to avoid the interpolation errors, since, based on Finite Element simulators, it uses the same grid to solve both the electrical and the optical equations and to study the propagation conditions.

1.1 Thesis organization

This thesis is, therefore, in the following manner structured:

- In the chapter 2, starting from a brief review on the guided propagation of the light, I remind the single mode condition for the planar waveguide (known as slab waveguide too) and the main and more general

method to study the 2D waveguides, and thus the rib waveguide too, the *Effective Index Method*.

- In the chapter 3 the basic physics effects, on which is based the main passive function of the integrated devices, the intensity and phase modulation, are exposed, since in my work I designed in particular an intensity modulator.

- In the chapter 4 I present and discuss the new criterion for the single-mode condition of the rib waveguides

- In the chapter 5 I show a device designed by means of the new, described simulation strategy. The device is an totally *Induced Bragg Reflector*(IBR) in a InP/InGaAsP *p-i-n* , based on the widely used field-effect in the InP derived material. Its innovative peculiarity is the anode electrode comb-structure. In fact it allows to induce the device in an unperturbed waveguide, by means of the applied electric field. What is interesting is into the induction of the device in the unperturbed waveguide or net of waveguides is the possibility 'to program', conformity with the necessity, several functions, like wavelength filtering, intensity modulation or, in a fan-configuration demultiplexing, or simply to chose the signal path. Moreover, I show that the IBR can work as intensity modulator for ultra-fast application, since it can potentially reach a transient response greater than 40 GHz, which is perfectly respondent to the actual request of the integrated modulators.

Chapter 2

Principles of Guided Light Waves

Nowadays the idea that the light can be confined in channels and in this manner transported where we want, and more that it can transport several information, is a concept that everyone has. The common people, which every day uses internet, whiteout any notion about the physics of the guided propagation of the light, knows that it is more convenient to diffuse the information and the data by means of the of optical fibers, since they are faster; have a greater capacity to carry a lot of data; are immune to electromagnetic perturbations and can be used along kilometers without have a significant signal reduction.

In this chapter we would like to give the basic concepts about the theory of the guided light in the dielectric medium.

After an intuitive exposition of the light confinement, we start recalling the Maxwell's equations in dielectric medium, to proceed then with their solutions in the simpler guiding structure, the planar waveguide, constituted by three layer of different dielectric material laid one on the top of the other. Of this structure we will analyze the propagation modes, or, in other worlds, we will see that assigned the thickness of the central layer, the refractive index profile and the propagating light wavelength, there exist only some defined propagation constant that can be supported by the waveguide. We finish with the illustration of a semi-analytical method to solve the Maxwell's equation in more complex structures, the two-dimensional waveguide.

2.1 Light Confinement

To have an intuitive picture of how it is possible to guide the light through a channel, we can recall in our mind the simple phenomenon which everyone has assisted in his life staying on the seashore or on a shore of a lake. We can see under the surface inside a range near us, but we cannot see anything if we look far: we see only the sky reflected on the water surface.

This happens because when a ray of light impinges an interface between to medium with different refractive index (that means with different density), coming from the medium with refractive index greater, like the water-air interface, a critical angle exist, such that for all the angle greater, the ray does not emerge in the other medium, but is totally reflected inside the origin medium: it is trapped inside this medium. In this manner the image of the object far from us is trapped in the water, since the rays coming from them to us have an incidence angle greater than the critical one.

This phenomenon is named *total internal reflection* (TIR) and was observed the first time in the far 1841 in a totally accidental way, how often happens in the physics history. A Swiss physicist, Daniel Colladon, during a hydraulic conference in a dark hall of the Geneva University, with the aim to illuminate the set-up of an experiment about the downflow and dispersion of the water by a little hole in the bottom of a basin, was using a metallic funnel to convey the sun light. Fortuitously, the sun light illuminated the hole with a suitable incidence angle and in the dark the water flow, going out, became bright: the light was trapped by the water thanks to subsequential reflections. In the same year an other physicist, the French Jacques Babinet, observed the same phenomenon illuminating the bottom of a bottle by means of a candle while he poured the liquid contained out. At that time the phenomenon appeared nice and spectacular but whiteout useful application, excepted the scenographic one (Colladon was invited by the 'Opera de Paris' to collaborate to the Gounoud's Faust scenography). Nevertheless Babinet suggested an interesting medical application: use glass barrets to illuminate the oral cavity, which was used at the end of the 18th century by two Viennese doctors, Roth and Reuss, and one American, David Smith, to patent some odontological instruments, which did not had a lot of success. Only in the second half of the twentieth century (when the name was coined), there was a revived interest about the guided light and its applications, which increased with the laser discovery, so that simultaneously there

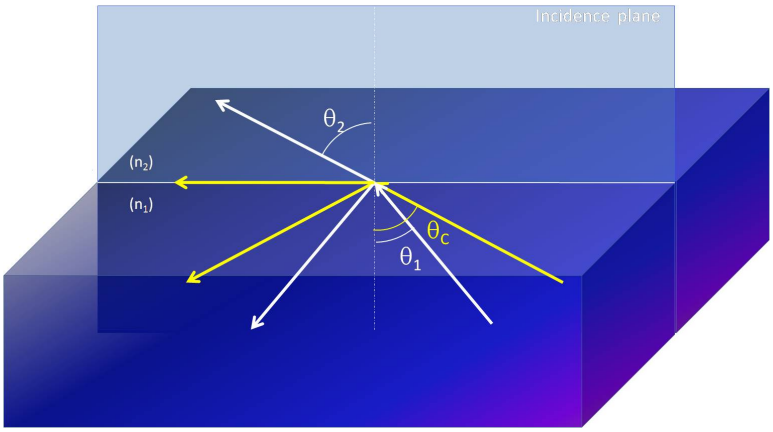

Figure 2.1: Reflection of the light rays at the interface between two medium with different density (corresponding to different refractive index). The rays, coming from the more dense medium (1) with an incidence angle θ_1, is partially reflected in the same medium with the same angle, and partially refracted in the second one through the interface with an refraction angle θ_2 greater than θ_1. As the incidence angle increases, the refraction angle approach to $\pi/2$, so that the refracted ray vanish. The correspondent incident angle is called *critical angle* and for all the angles of incidence greater than this one, the ray is only reflected inside the origin medium. This phenomenon is named *Total Internal Reflection* and is the basic phenomenon of the guiding light theory.

was an exponentially rate of progress.

After this historical divagation, we can conclude that to trap the light in a channel, the refractive index of the channel must be bigger than the refractive index of the surrounding medium, like in the case of water or glass channel in air.

The critical angle can be easily derived from the Descartes formulation of the Snell's Law, illustrated by the figure 2.1,

$$n_1 \sin\theta_1 = n_2 \sin\theta_2. \tag{2.1}$$

Since $n_1 > n_2$ implies $\theta_1 < \theta_2$, as the θ_1 angle increases, the angle θ_2 will approach to 90°, which means that there is not refracted ray, but only reflected. This corresponds to put in the (2.1) the condition $\theta_2 = \pi$, so that the critical angle is determined:

$$\theta_c = \arcsin\frac{n_1}{n_2}. \tag{2.2}$$

The previous relation seems suggest that the light can propagate in a waveguide with all the angle greater than the critical angle. It is not true. The light in a waveguide can propagate only with some determined angles, depending on its wavelength and on waveguide geometry. It is possible show this by means of a simple ray optics approach, but to fully show the basic property of the guided light, we resort to the Maxwell's equation.

2.2 Maxwell's equations in homogeneous dielectric medium

In the more general case of a propagation of the electromagnetic field in a medium, in addition to the *electric filed* $\mathbf{E}$ and the *magnetic field* $\mathbf{H}$, the Maxwell's equations, involve others two fields, the *electric displacement vector*, $\mathbf{D}$, and the the *magnetic flux density vector*, $\mathbf{B}(\mathbf{r}, t)$, which contain the effects of the external electromagnetic field on the medium, i.e. the matter polarization and magnetization

$$\nabla \cdot \mathbf{D}(\mathbf{r}, t) = \rho \tag{2.3a}$$

$$\nabla \cdot \mathbf{H}(\mathbf{r}, t) = 0 \tag{2.3b}$$

$$\nabla \times \mathbf{E}(\mathbf{r}, t) = -\frac{\partial \mathbf{B}(\mathbf{r}, t)}{\partial t} \tag{2.3c}$$

$$\nabla \times \mathbf{H}(\mathbf{r}, t) = \mathbf{J} + \frac{\partial \mathbf{D}(\mathbf{r}, t)}{\partial t}, \tag{2.3d}$$

where ρ is the *density charges* outside the medium and $\mathbf{J}$ is the *current density*.

To unambiguously determine the field vectors given by a distribution of currents and charges, we need to relate the vectors $\mathbf{D}$ and $\mathbf{J}$ to the field $\mathbf{E}$ and the field $\mathbf{B}$ to $\mathbf{H}$. These relations depend on the material and are usually called *constitutive relations* or *material relations*. In the case of a *linear* and *isotropic* medium, i.e., if the intensities of the fields are not so strong and if the medium physical properties do not depend on the field direction, the constitutive relations are:

$$\mathbf{D} = \epsilon \mathbf{E} \tag{2.4a}$$

$$\mathbf{B} = \mu \mathbf{H} \tag{2.4b}$$

$$\mathbf{J} = \sigma \mathbf{E}, \tag{2.4c}$$

where ϵ is the *electric permittivity*, or (*dielectric constant* for linear materials), μ the *magnetic permeability* and σ the *conductivity*, characteristics of the materials.

Most of the materials used in optoelectronics to realize waveguides and others devices with their substrate are perfect insulant (*dielectric*), so that their conductivity is $\sigma \approx 0$. For these materials, considering no others charges and currents in the space, ($\mathbf{J} = 0$ and $\rho = 0$),using the (2.4), the equations Maxwell's equations (2.3) become:

$$\nabla \mathbf{E}(\mathbf{r}, t) = 0 \tag{2.5a}$$

$$\nabla \mathbf{H}(\mathbf{r}, t) = 0 \tag{2.5b}$$

$$\nabla \times \mathbf{E}(\mathbf{r}, t) = -\frac{\partial \mu \mathbf{B}(\mathbf{r}, t)}{\partial t} \tag{2.5c}$$

$$\nabla \times \mathbf{H}(\mathbf{r}, t) = \frac{\partial \epsilon \mathbf{E}(\mathbf{r}, t)}{\partial t} \tag{2.5d}$$

and after some mathematical manipulations, they are reduced to a system of only two equations for the electric and magnetic fields:

$$\nabla^2 \mathbf{E} - \mu\epsilon \frac{\partial^2 \mathbf{E}}{\partial t^2} + (\nabla \ln \mu) \times (\nabla \times \mathbf{E}) + \nabla(\mathbf{E} \cdot \nabla \ln \epsilon) = 0 \tag{2.6a}$$

$$\nabla^2 \mathbf{H} - \mu\epsilon \frac{\partial^2 \mathbf{H}}{\partial t^2} + (\nabla \ln \epsilon) \times (\nabla \times \mathbf{H}) + \nabla(\mathbf{H} \cdot \nabla \ln \mu) = 0. \tag{2.6b}$$

For *homogeneous* materials, which have the electric permittivity and the magnetic permeability independent on position, so that $\nabla \ln \epsilon = \nabla \ln \mu = 0$, the previous system assumes the simple form of a system of two uncoupled differential equations in partial derivatives for the fields $\mathbf{E}$ and $\mathbf{H}$

$$\nabla^2 \mathbf{E} = \mu\epsilon \frac{\partial^2 \mathbf{E}}{\partial t^2} \tag{2.7a}$$

$$\nabla^2 \mathbf{H} = \mu\epsilon \frac{\partial^2 \mathbf{H}}{\partial t^2} \tag{2.7b}$$

which correspond to a set of six scalar equations, with the well known mathematical form of the *waves equations*, for each cartesian component, $A_j = E_j, H_j$, with $j = x, y, z$, of the fields $\mathbf{E}$ and $\mathbf{H}$

$$\nabla^2 A_j = \mu\epsilon \frac{\partial^2 A_j}{\partial t^2} \tag{2.8}$$

.

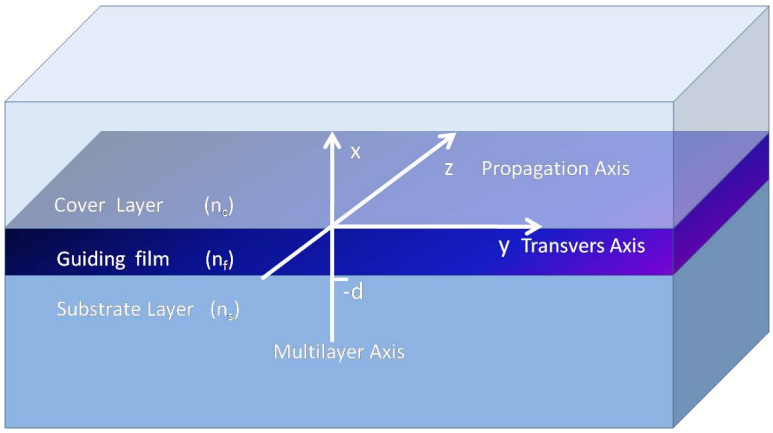

Figure 2.2: Three layers planar waveguide.

This suggest that the electromagnetic field in the dielectric materials propagates as a wave with velocity

$$v = \frac{1}{\sqrt{\epsilon\mu}}. \tag{2.9}$$

Usually is preferred to refer this velocity to the electromagnetic waves speed in the vacuum, defined as $c = 1/\sqrt{\epsilon_0\mu_0}$ (ϵ_0 is the *vacuum permittivity* and μ_0 the *vacuum magnetic permeability*), defining

$$v \equiv \frac{c}{n}. \tag{2.10}$$

The previous relation defines the *refractive index*, n, of the materials as a quantity which expresses how fast is the electromagnetic wave in the material: greater is the refractive index and slower is the propagation, or, in other words, greater is the delay cumulated by a monochromatic component of the field in the material.

2.3 Wave Equations in dielectric Planar Waveguides

To better understand how it is possible to confine the light waves in a guide and their main features, we can solve the wave equation in the simpler structure possible, the *planar waveguide*, shown in figure 2.2.

The structure consists of a non magnetic dielectric film (magnetic permeability $\mu = 0$, and conductivity $\sigma = 0$), with refractive index n_f, sandwiched between to non magnetic dielectric media, the substrate and the cover, with

different refractive index, n_s and n_c respectively. We suppose, further, these refractive indices slightly changing along the direction orthogonal to the sandwich axis (x axis in figure) only, so that in each region is

$$\nabla \ln \epsilon = \nabla \ln \mu \approx 0. \tag{2.11}$$

We will see that the confinement is possible inside the film, i.e. along the direction normal to the film plane. The case of confinement in two direction (*channel waveguide*) is easily derived from this one, while the other more complicated geometry and the case of inhomogeneous media, present only mathematical complication, which adds nothing to the comprehension of the basic physic of the waveguides.

Although the whole structure is inhomogeneous along one direction (x in the figure), we can resort to the wave equations (2.7) in each quasi-homogeneous region (subsisting the condition (2.11)), limiting our observation only to monochromatic waves with angular frequency ω and phase front orthogonal to the structure axis (z), we can suppose the fields intensity dependent only on x coordinate

$$\mathbf{A}(x,t) = \mathbf{A}(x)e^{i(\omega t - \beta z)} \tag{2.12}$$

Given the refractive index distribution $n(x)$, which defines the waveguide geometry, this reduce the problem to solve the system of 6×3 equations, one for each cartesian component of the fields, $A_l(x)$ ($A = E, H$ and $l = x, y, z$), in each of the three regions:

$$\left[\frac{\partial^2}{\partial x^2} + (k^2 n_j^2 - \beta^2)\right] A_{jl}(x) = 0 \tag{2.13}$$

(where $j = s, f, c$ in the substrate, in the film and in the cover respectively) imposing the continuity to the fields tangential components at the dielectrics interface. In the latter equation $k = 2\pi\lambda$ is the *wave number*, being $\lambda = 2\pi c/\omega$ the *wavelength* and, we used the (2.9) and (2.10).

Obviously the solutions of each equations of the previous system are not independent since they are related each to others from the Maxwell's equations. This is a lot advantageous if we image to have an incident wave with one between the two fields, for example the electric (magnetic), polarized along the direction parallel to the film plane (y axis), so that the other field, the magnetic (electric), has only the others two orthogonal components x and z (we remember that are considering plane waves defined by the (2.12). In

this case, in fact, the previous system is reduced at only three equations, but we can solve only that involving E_y (H_y), and derive the others component of the electro-magnetic field directly from the Maxwell's equations.

To be explicit, if we have a wave such that is $\mathbf{E}(x) = (0, E_y(x), 0)$, and $\mathbf{H}(x) = (H_z(x), 0, H_z(x))$ the system to solve is:

$$\left[\frac{d^2}{dx^2} + (k^2 n_j^2 - \beta^2)\right] E_{yj}(x) = 0 \tag{2.14a}$$

$$H_{xj} = -(\beta/\omega\mu_0) E_{yj} \tag{2.14b}$$

$$H_{zj} = (i/\omega\mu_0)\partial E_{yj}/\partial x \tag{2.14c}$$

with continuity conditions for the fields and their first derivatives at dielectric interface ($x = 0$,$x = -d$). From figure we see that is

$$j = \begin{cases} c & \forall x \geq 0 \\ f & \forall -d < x < 0 \\ s & \forall x < -d \end{cases} \tag{2.15}$$

In the complementary case we have an electro-magnetic field $\mathbf{H}(x) = (0, H_y(x), 0)$
$\mathbf{E}(x) = (E_z(x), 0, E_z(x))$, so that the system to solve is

$$\left[\frac{d^2}{dx^2} + (k^2 n_j^2 - \beta^2)\right] H_{yj}(x) = 0 \tag{2.16a}$$

$$E_x = -(\beta/\omega\epsilon_0 n_j^2) H_y \tag{2.16b}$$

$$E_z = (1/i\omega\epsilon_0 n_j^2)\partial H_y/\partial x \tag{2.16c}$$

Waves like the (2.14), which have only the transversal component of the electric field, are known as *transverse electric modes* of the planar waveguide (TE modes) ('transversal' is referred to the incident plane of the wave which is along the y axis in the case we are considering, illustrated in figure 2.3), while waves like the (2.16), which have only the component transversal of the magnetic field (see on the left of figure 2.3), are known as *transverse magnetic modes* (TM modes). They constitute a base of the solutions space of the the system (2.13).

At this point we note that a general solution of the (2.13) is

$$A_j(x) = \mathcal{A}_j e^{i\gamma_j x} + \mathcal{B}_j e^{-\gamma_j x} \tag{2.17}$$

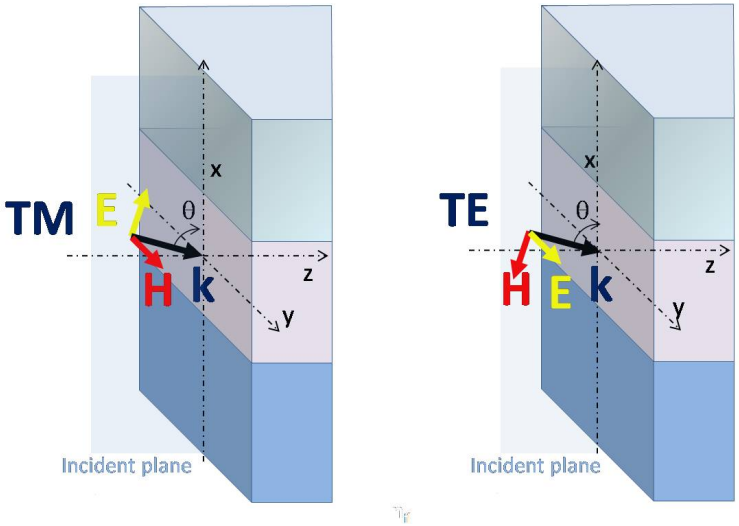

Figure 2.3: TM polarization (left) and TE polarization (right) of the electromagnetic field in a planar waveguide.

being

$$\gamma_j = \sqrt{k_0^2 n_j^2 - \beta^2} \tag{2.18}$$

Defining the *effective refractive index*, N, as a quantity such that

$$\beta = k_0 N \tag{2.19}$$

we can establish the guided conditions in terms of refractive index. Indeed, assuming that

$$n_s < n_c < n_f \tag{2.20}$$

we have:

1. **not physically solution** if

$$n_c < N \tag{2.21}$$

   since this corresponds to exponential solutions in each of the three layers (γ_j imaginary $\forall j = c, f, s$), therefore to waves that carry an infinite energy at infinity.

2. **guided modes** (i.e., *confined modes*) in the film if is:

$$n_s < N < n_f, \tag{2.22}$$

corresponding to sinusoidal solutions of the wave equations in the film with exponentially decadent tails in the cover and substrate (to have physically solutions in the sense previous specified, we have to put $\mathcal{A}_c = 0$ and $\mathcal{B}_s = 0$;

3. **substrate modes** if
$$n_c < N < n_s < n_f \tag{2.23}$$
corresponding to sinusoidal solutions in the film and substrate with evanescent tails in the cover;

4. **radiation modes**, corresponding to sinusoidal waves in each layer, if
$$N < n_c. \tag{2.24}$$

2.3.1 TE guided modes

In the next we will give an explicit form to the TE modes.

Fulfilled the condition of the case 2 and imposed the continuity of the fields and their first derivative at dielectric interfaces $x = 0$ and $x = -d$

$$E_{yc}(0) = E_{yf}(0) \tag{2.25a}$$
$$E_{yf}(-d) = E_{ys}(-d) \tag{2.25b}$$
$$E'_{yc}(0) = E'_{yf}(0) \tag{2.25c}$$
$$E'_{yf}(-d) = E'_{ys}(-d), \tag{2.25d}$$

with similar for $H_z(x)$, putting the (2.25) in the (2.17), we have a system of four equation with five unknown parameters $\mathcal{B}_c$, $\mathcal{A}_f$, $\mathcal{B}_f$, $\mathcal{A}_s$ and β. Leaving the first one as free parameter (which could be settled by the energy), we arrive to the following *dispersion relation* for asymmetric step-index planar waveguide:

$$\tan \gamma_f d = \frac{\dfrac{\gamma_c + \gamma_s}{\gamma_f}}{1 - \dfrac{\gamma_c \gamma_s}{\gamma_f^2}} \tag{2.26}$$

The latter transcendental equation defines the propagation constant β as implicit function of the waveguide parameters (the refractive indices, n_f, n_c, n_s, and the guide thickness, d), and of the working wavelength, λ. It imposes a β quantization, since the left member, being a tangent function, fulfils

$$\tan \gamma_f d = \tan \gamma_f d + m\pi \quad m \in Z \tag{2.27}$$

So that exist several β_m for each solution of the (2.26). In others words, assigned the refractive index profile and the working wavelength, a waveguide can support several modes (*multi-mode waveguides*) individuated by the integer m, called *mode order*. Generally the number of the supported modes is finite. In a particular case that the waveguide supports only the mode $m = 0$, we speak of *mono-mode waveguide*. In some others cases, for particulary values of the wavelength, the waveguide cannot support any modes, and we say that the waveguide is in *cut-off*. We will discuss in details in the next, the single mode and cut-off conditions.

To design a waveguide is more comfortable define some dimensionless parameters, known as *normalized parameters*

$$b = \left(N^2 - n_s^2\right) / \left(n_f^2 - n_s^2\right) \qquad \text{Normalized mode index} \tag{2.28}$$

$$V = k_0 d \sqrt{n_f^2 - n_s^2} \qquad \text{Normalized film thickness} \tag{2.29}$$

$$a = \left(n_s^2 - n_c^2\right) / \left(n_f^2 - n_s^2\right) \qquad \text{Asymmetry measure} \tag{2.30}$$

For a guided mode, since subsist the (2.22), is $0 < b < 1$; the normalized thickness gives, instead, the physic thickness of the film as function of the guided wavelength, assigned the refractive index step between the film and the substrate; obviously the asymmetry measure is zero for $n_c = n_s$ and increase with the difference between these two indices.

The (2.26) in terms of the previous parameters becomes:

$$\tan\left[V\sqrt{1-b}\right] = \frac{\dfrac{\sqrt{b} + \sqrt{b+a}}{\sqrt{1-b}}}{1 - \dfrac{\sqrt{b(b+a)}}{1-b}} \tag{2.31}$$

The determination of the propagation constant β from the (2.26) (or of the normalized mode index b from the (2.31)) allows to make explicit the electric field in the three regions:

$$E_y(x) = \begin{cases} \mathcal{B}_c e^{\gamma_c x} & x \geq 0 \\ \mathcal{B}_c \left(\cos \gamma_f x - \dfrac{\gamma_c}{\gamma_f} \sin \gamma_f x \right) & -d < x < 0 \\ \mathcal{B}_c \left(\cos \kappa_f d + \dfrac{\gamma_c}{\gamma_f} \sin \gamma_f x \right) e^{\gamma_s (x+d)} & x \leq -d \end{cases} \tag{2.32}$$

The previous explicit expression of the field shows as it decreases exponentially in the cover and substrate with penetration depth $\mid \gamma_c^{-1} \mid$ and $\mid \gamma_s^{-1} \mid$ respectively. We note from (2.18) and (2.20) that the penetration is lower in the cover than in the substrate since there the refractive index is lower, and it increases with the mode order due to the decrease of the propagation constant. This means that higher is the mode order and higher are the penetration in the lateral region of the guide, while in the guided region the number of the field amplitude distribution nodes increases, so that we have an increasing number of intensity spot in the cross section of the guide.

2.3.2 TM guided modes

As in the case of TE modes, applying the right condition at dielectric interface we arrive at the *dispersion relation* for TM modes

$$\tan\left[V\sqrt{1-b}\right] = \frac{\dfrac{1}{\gamma_1}\sqrt{\dfrac{b}{1-b}} + \dfrac{1}{\gamma_2}\sqrt{\dfrac{b+a}{1-b}}}{1 - \dfrac{1}{\gamma_1\gamma_2}\dfrac{\sqrt{b(b+a)}}{(1-b)}} \tag{2.33}$$

where we have defined $\gamma_1 \equiv (n_s/n_f)^2$ and $\gamma_2 \equiv (n_c/n_f)^2 = \gamma_1 - a(1-\gamma_1)$.

The explicit solution for the magnetic field is

$$H_y(x) = \begin{cases} \mathcal{B}_c e^{-\gamma_c x} & x \geq 0 \\ \mathcal{B}_c \left(\cos\gamma_f x - \dfrac{n_f^2\gamma_c}{n_c^2\gamma_f} sin\gamma_f x \right) & -d < x < 0 \\ \mathcal{B}_c \left(cos\gamma_f d + \dfrac{n_f^2\gamma_c}{n_c^2\gamma_f} sin\gamma_f d \right) e^{\gamma_s(x+d)} & x \leq -d \end{cases} \tag{2.34}$$

The behavior is similar to the case of TE modes except the discontinuity at dielectric interface ($x = 0$ and $x = -d$) due to the step change of the refractive index, so that for the guided mode the energy is confined in the film with evanescent tails in the lateral regions that increase with the increase of the mode order.

2.3.3 Guided Modes Cut Off

For each mode, given the wavelength of the propagating light, there exists a minimum value of the film thickness starting from which the mode can be

supported. This happens when $N \longrightarrow n_s$, since from the (2.28) we see that

$$b = \left(N^2 - n_s^2\right) / \left(n_f^2 - n_s^2\right) \xrightarrow{N \longrightarrow n_s} 0 \tag{2.35}$$

The corresponding normalized film thickness for the *m-th* TE and TM mode are

$$V_{mTE}^{CO} = \arctan\sqrt{a} + m\pi \tag{2.36}$$

$$V_{mTM}^{CO} = \arctan(\sqrt{a}/\gamma_2) + m\pi \tag{2.37}$$

The condition (2.20) leads to

$$V_{mTM}^{CO} > V_{mTE}^{CO} \tag{2.38}$$

which means that if the *m-th* TE mode is in *cut-off*, the correspondent TM mode is in *cut-off* too, but is not true the opposite.

For symmetric planar waveguide ($a = 0$) is

$$V_{mTM}^{CO} = V_{mTE}^{CO} = m\pi, \tag{2.39}$$

which means that at least the fundamental modes can propagate.

2.4 2D waveguides

It easy to image that the planar waveguide cannot be used in the real case. Infinite structures are not realizable and even if a waveguide with planar dimension greater an greater than the film width can be mathematically considered as infinite (and thus it can be approximate to an ideal planar waveguide) a similar structure first of all does not marriage the request of high integrability of the devices. The main consideration, nevertheless, is that the energy (equivalently, the information) must be confined in the space to be carried, so that the waveguides really used in the devices are *channel waveguides*, or more often, *rib waveguides*. The main types are shown in figure 2.4.

The first one, from left to right, is a channel waveguide, where upon a substrate is deposited the guiding film whit refractive index greater, and then totally etched to build the channel. The second one is a buried channel waveguide, which the substrate is etched to receive the guiding medium deposited and buried under the cover layer. The last one is a rib waveguide,

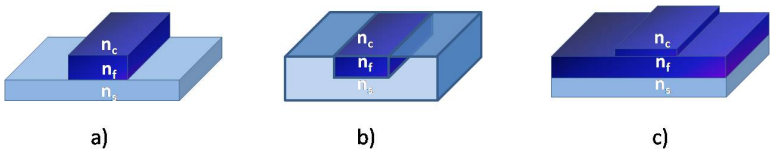

Figure 2.4: Main types of 2D waveguides: a) channel waveguide b) buried channel waveguide; c) rib waveguide. Assured the confinement condition, $n_c \leq n_s < n_f$, the light propagation is confined in the channel (a and b), below the ribbed region (c).

as the name suggests, which is made by etching the guiding film deposited upon the substrate and leaving only a rib on the guiding layer.

In these waveguides the refractive index changes along both the directions orthogonal to the propagation axis z, so that the confinement, assured the condition (2.20), happens inside the channel, which is constituted by the region below the rib, in the case of the rib waveguide. As consequence the waveguides modes have not a well defined polarization like the TE and TM modes of the planar waveguides. Fortunately these modes are strongly polarized along the x and y axes. They are called *transversal electromagnetic modes* (TEM) and between them, the modes mainly polarized along the x axis are called *quasi-TM modes*, since they are very similar to the TM modes of the planar waveguides. Usually they are simple called E^x_{qp} modes, whit obvious meaning of the x apex, while the subscripts p and q indicate the number of nodes of the electric field E_x along the x and y direction, respectively. The others modes polarized mainly along the y direction, being similar to the TE modes of the planar waveguides, are called *quasi-TE modes* or simply E^y_{qp}.

Taking into account with we have just said, to find the 2D-waveguides modes we can search general solutions of the Maxwell's equations with amplitude depending only on x and y

$$\mathbf{E}(x, y, z, t) = \mathbf{E}(x, y)e^{i(\omega t - \beta z)} \tag{2.40}$$

$$\mathbf{H}(x, y, z, t) = \mathbf{H}(x, y)e^{i(\omega t - \beta z)} \tag{2.41}$$

and, advancing as in the case of planar waveguides, we can express the transverse components of the fields as functions of their longitudinal components

$$E_x = -(i/K_j^2)[\beta(\partial E_z/\partial x) + \omega\mu_0(\partial H_z/\partial y)] \tag{2.42a}$$
$$E_y = -(i/K_j^2)[\beta(\partial E_z/\partial y) - \omega\mu_0(\partial H_z/\partial x)] \tag{2.42b}$$

$$H_x = -(i/K_j^2)[\beta(\partial H_z/\partial x) - \omega n_j^2\epsilon_0(\partial E_z/\partial y)] \tag{2.43a}$$
$$H_y = -(i/K_j^2)[\beta(\partial H_z/\partial y) + \omega n_j^2\epsilon_0(\partial E_z/\partial x)] \tag{2.43b}$$

where the parameter K_j is defined by:

$$K_j^2 = n_j^2 k_0^2 - \beta^2 \tag{2.44}$$

with $k_0 = \omega\epsilon_0\mu_0$, being ω the angular frequency of the light.

The longitudinal components of the fields E_z and H_z must be derived from the following wave equations

$$\begin{aligned}\left[\frac{\partial^2}{\partial x^2} + \frac{\partial^2}{\partial y^2} - \left[\beta^2 - k_0^2 n^2(x,y)\right]\right] E_z = 0 \\ \left[\frac{\partial^2}{\partial x^2} + \frac{\partial^2}{\partial y^2} - \left[\beta^2 - k_0^2 n^2(x,y)\right]\right] H_z = 0\end{aligned} \tag{2.45}$$

taking into account the appropriate boundary conditions at dielectric interfaces.

Unfortunately the previous problem has not an analytic solution. We must resort to numerical methods. The commonly used are the Marcatili's method [24] and the Effective Refractive Index method (EIM) [25]. The second one is the more general, since it could be used even in the case of non uniform refractive index of the waveguide core (the guiding region). In the next we will explain it in the simple case of a channel waveguide.

2.4.1 Effective Index Method

The Effective Index Method is an approximate method to compute the propagation modes of the 2D-waveguides, or, in mathematical therm, to solve the eigenvalues problems (2.4). It is very simple to apply since it reduces the problem to solve sequentially several 1D problem. The logic of the method is well expressed by the scheme of figure 2.5, where a simple case of a channel waveguide is presented. The channel waveguide with height H and width w

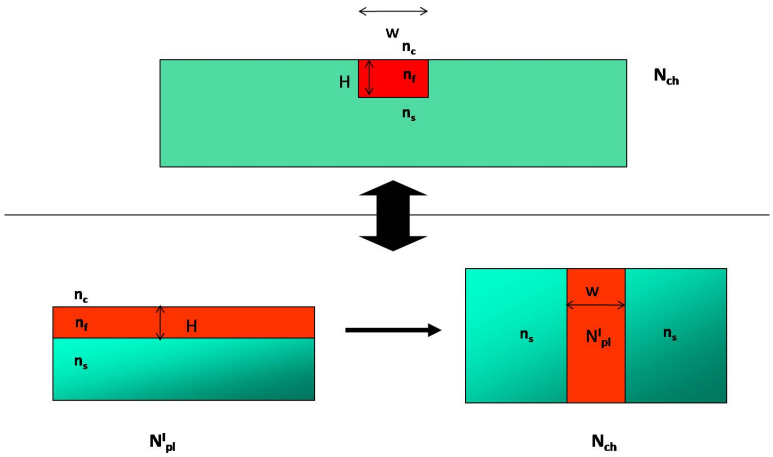

Figure 2.5: Illustration of the *Effective Index Method* for a channel waveguide. The channel waveguide, with height H and width w, is decomposed in two fictitious planar waveguides. The first one with the same height H and with the same cover and substrate of the channel. Once the effective refractive index, N_{pl}^{I}, of this waveguide is calculated, a second fictitious planar waveguides is considered, with the same width w of the channel, but with refractive index in the guiding film equal to N_{pl}^{I}. The surrounding material is the lateral material of the channel. In the considered case it is the substrate. The solution of the wave equation for the second fictitious planar waveguide, gives us a good approximation of the effective refractive index of the planar waveguide.

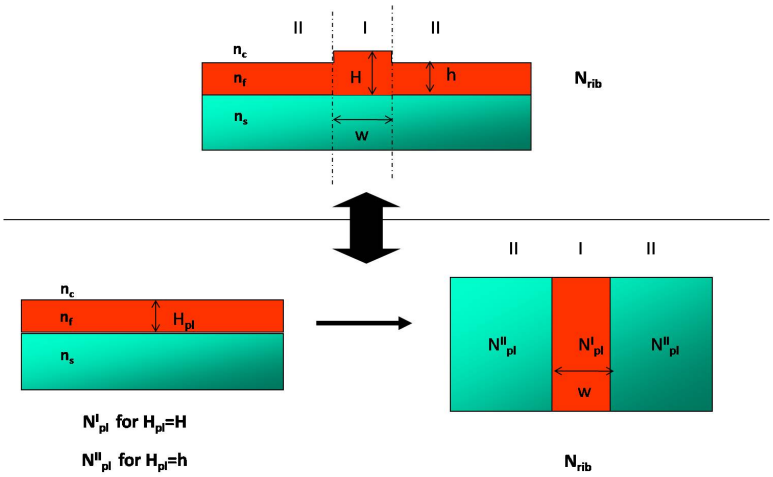

Figure 2.6: Illustration of the *Effective Index Method* for a rib waveguide. The rib waveguide is subdivided in three regions, one central region and two lateral regions, so that the effective refractive indexes, N_{pl}^{I} and N_{pl}^{II}, of two fictitious planar waveguides with film height equal to the total height of the ribbed region, H, and equal to the height of the lateral planar regions, h, respectively, are calculated. These effective refractive indexes are than used as refractive indexes in an other fictitious planar waveguides to determine the effective refractive index of the rib waveguide.

is decomposed in two fictitious planar waveguides. The first one with the same height H and same surrounding materials, i.e. the same upper cover and the same substrate, of the channel. Once the effective refractive index, N_{pl}^{I}, of this waveguide is calculated, a second fictitious planar waveguides is considered, with the same width w of the channel, but with refractive index in the guiding film equal to the effective refractive index of the first fictitious planar waveguides. The surrounding material is the lateral material of the channel. In the considered case of the figure 2.5 it is the substrate. If we consider a waveguide with the channel surrounded by the cover, the surrounding material must be the cover. The solution of the wave equation for the second fictitious planar waveguide, gives us a good approximation of the effective refractive index of the planar waveguide.

Obviously the case of the rib waveguides is more complicate, since the guiding region (the region below the rib) is surrounded by non uniform regions. In this case the problem is decomposed in more than two steps. The rib waveguide is subdivided in three regions: one central and two lateral, so that the effective refractive indexes of two fictitious planar waveguides, with

film height equal to the total height of the ribbed region, H, and equal to the height of the lateral planar regions, h, respectively (figure 2.6), are calculated. These effective refractive indexes are than used as refractive index in an other fictitious planar waveguides to determine the effective refractive index of the rib waveguide.

Care must be taken to consider the polarization involved, since the sequential fictitious planar waveguides are taken with orthogonal axes. This implies that if we are considering an electric field polarized along the x axis, we have to solve the TM wave equation for the first three layers fictitious planar waveguide and the TE wave equation for the second fictitious three layer planar waveguide, since the considered electric field have a TE polarization respect to this waveguide.

Mathematical the problem is formulated in this manner: starting from the basic assumption that the solutions of the (2.4) can be factorized as:

$$A(x,y) = \Theta(x,y)\Phi(y), \tag{2.46}$$

with the approximation that the $\Theta(x,y)$ function has slowly change respect the y coordinate. This leads to two independent wave equations for the Θ and Φ functions

$$\left[\frac{\partial^2}{\partial x^2} - \left[N(y)^2 - k_0^2 n^2(x,y)\right]\right]\Theta(x,y) = 0 \tag{2.47}$$

$$\left[\frac{\partial^2}{\partial y^2} - \left[\beta^2 - k_0^2 N(y)^2\right]\right]\Phi(y) = 0, \tag{2.48}$$

where it is clear that the first one is parametric in y, so that the eigenvalue N is a function of y. The procedure to solve these equation is the same illustrated in the section 2.3.

2.5 Anisotropic Materials

The constitutive equations (2.4) say that in the isotropic medium the polarization of the field inside the material is in the same direction of the electric field which has induced it. Otherwise in the anisotropic medium, which have the *electric permittivity* dependent on the propagation direction. This means that the displacement vector $\mathbf{D}$ and the electric field $\mathbf{E}$ are not necessarily

parallel and thus mathematically related each to the others by means of a tensor, so that for their cartesian components the following relation subsists:

$$D_k = \epsilon_{kl} E_l, \tag{2.49}$$

where obviously $k, l = x, y, z$, and the Einstein's formalism for the summation is adopted, according to whit there is summation over repeated indices.

An electric permittivity dependent on the direction implies that the refractive index experienced by the propagating field inside the material, depend on the propagation direction too. Let us see the consequences.

2.5.1 Propagation inside anisotropic media

Let us consider a monochromatic plane waves, with radiant frequency ω, propagating inside an anisotropic crystal along an arbitrary direction $\mathbf{s}$

$$\mathcal{E} = \mathbf{E} e^{i\left(\omega t - \omega \frac{n}{c} \mathbf{r} \cdot \mathbf{s}\right)}, \tag{2.50}$$

where c is the light speed and n is the refractive index of the material. The wave vector is thus $\mathbf{k} = (\omega n/c)\mathbf{s}$. For this wave, supposing absence of charges, we can write the Maxwell's equations (2.3c) and (2.3d) as:

$$\mathbf{D} = -\frac{n}{c} \mathbf{s} \times \mathbf{H} \tag{2.51}$$

$$\mathbf{H} = \frac{n}{\mu c} \mathbf{s} \times \mathbf{E} \tag{2.52}$$

(we remaind that μ is the *magnetic permeability* of the medium). This means that in the crystal both $\mathbf{D}$ and $\mathbf{H}$ are orthogonal to $\mathbf{s}$, and perpendicular each others, while $\mathbf{E}$ is orthogonal to $\mathbf{H}$ but not to $\mathbf{s}$ and, as observed at the begin of this section, is not parallel to $\mathbf{D}$. In particularly, different from the isotropic medium, the direction of the energy flow, given by the Poynting vector $\mathbf{E} \times \mathbf{H}$, is not collinear with the direction of the phase propagation $\mathbf{s}$.

From the previous equation, resorting to the vector identity $\mathbf{a} \times (\mathbf{b} \times \mathbf{c}) = \mathbf{b}(\mathbf{a} \cdot \mathbf{c} - \mathbf{c}(\mathbf{a} \cdot \mathbf{b})$, we obtain

$$\mathbf{D} = \frac{n^2}{c^2 \mu} \left[\mathbf{E} - \mathbf{s} \left(\mathbf{s} \cdot \mathbf{E}\right)\right] = \frac{n^2}{c^2 \mu} E_{transverse} \tag{2.53}$$

using then the (2.49), considering that $n^2/(c^2\mu) = \epsilon_0$ and since $\mathbf{D} \cdot \mathbf{s} = 0$ we obtain

$$E_k = \frac{n^2 s_k \left(\mathbf{s} \cdot \mathbf{E}\right)}{n^2 - \epsilon'_k}, \tag{2.54}$$

where $k = x, y, z$ and the *relative dielectric constants* $\epsilon'_k \equiv \epsilon_k/\epsilon_0$ has been defined. Multiplying by s_k and summing over k we arrive easily to the following quadratic equation in n^2, named only after Fresnel,

$$\frac{s_x^2}{n^2 - \epsilon'_x} + \frac{s_y^2}{n^2 - \epsilon'_y} + \frac{s_z^2}{n^2 - \epsilon'_z} = \frac{1}{n^2}. \tag{2.55}$$

The two admitted solutions $\pm n_1$ and $\pm n_2$ (the sign correspond to the reverse phase velocity) are the refractive indices experienced by the two allowed independent plane wave propagations in the crystal. To find the amplitudes of this waves, the system (2.54) must be solved replacing on at time n_1 and n_2.

2.5.2 Index Ellipsoid

To describe the propagation inside the anisotropic medium, in the practice the (2.55) and (2.54) are not used. A merely mathematical construction, which easily, assigned the propagation direction of the electric field inside the crystal, gives the refractive index seen by the field along that direction, is useful. It is derived starting from the *stored electric energy density*, w, which, considering the (2.49), results to be

$$w = \frac{1}{2}\mathbf{E} \cdot \mathbf{D} = \frac{1}{2} E_k \epsilon_{kl} E_l. \tag{2.56}$$

Deriving it respect to the time, we can demonstrate that the dielectric tensor, ϵ, has only six independent component.

$$\dot{w} = \frac{\epsilon_{kl}}{2}\left(\dot{E}_k E_l + E_k \dot{E}_l\right). \tag{2.57}$$

In fact, if we consider the power flow per unit volume in the medium, which by the Maxwell's equation we can write as

$$\nabla \cdot (\mathbf{E} \times \mathbf{H}) = \mathbf{E} \cdot \dot{\mathbf{D}} + \mathbf{H} \cdot \dot{\mathbf{B}}, \tag{2.58}$$

we have that the first term at right side of the previous equation must be equal to $\dot{w}$, so that, rewriting this term using the (2.49), we obtain:

$$\frac{\epsilon_{kl}}{2}\left(\dot{E}_k E_l + E_k \dot{E}_l\right) = E_k \epsilon_{kl} D_l. \tag{2.59}$$

The previous equation is satisfied only if

$$\epsilon_{kl} = \epsilon_{lk},$$

which means that the dielectric tensor is symmetric, so that the energy density becomes

$$2w = \epsilon_{xx}E_x^2 + \epsilon_{yy}E_y^2 + \epsilon_{zz}E_z^2 + 2\epsilon_{xy}E_xE_y + 2\epsilon_{yz}E_yE_z + 2\epsilon_{zx}E_zE_x \quad (2.60)$$

Using an suitable axis transformation, we can diagonalize the ϵ tensor. The axis x, y and z, respect to which this diagonalization happens are called *principal dielectric axes* of the crystal and respect them the equation (2.60) becomes

$$2w = \epsilon_x E_x^2 + \epsilon_y E_y^2 + \epsilon_z E_z^2. \quad (2.61)$$

To reach our initial goal, we have to rewrite the previous expression in terms of the displacement vector D, that is

$$2w = \frac{D_x^2}{\epsilon_x} + \frac{D_y x^2}{\epsilon_y} + \frac{D_y^2}{\epsilon_y}, \quad (2.62)$$

since in the new system of coordinates is

$$\begin{bmatrix} D_x \\ D_y \\ D_z \end{bmatrix} = \begin{bmatrix} \epsilon_x & 0 & 0 \\ 0 & \epsilon_y & 0 \\ 0 & 0 & \epsilon_z \end{bmatrix} \begin{bmatrix} E_x \\ E_y \\ E_z \end{bmatrix}. \quad (2.63)$$

The (2.62) shows that in the D_x, D_y, D_z space, the the constant energy surfaces w_l inside the medium are ellipsoids. This ellipsoid is what we need to describe the propagation inside the anisotropic medium.

In fact if we replace $\mathbf{D}/\sqrt{2w\epsilon_0}$ by $\mathbf{r}$ and defining the refractive indices along the principal axis by

$$n_k^2 \equiv \epsilon_k' = \epsilon_k/\epsilon_0, \quad (2.64)$$

from the (2.62), we obtain the equation of an ellipsoid with the principal axis along the principal axes of the crystal, whose respective length are $2n_x$, $2n_y$ and $2n_z$

$$\frac{x^2}{n_x^2} + \frac{y^2}{n_y^2} + \frac{z^2}{n_z^2} = 1. \quad (2.65)$$

This ellipsoid is known as the *index ellipsoid* or *optical indicatrix* and, assigned a propagation direction, $\mathbf{s}$, it is useful to individuate, in a graphical manner, the two refraction indices and the corresponding direction of $\mathbf{D}$ associates with the two independent plane waves that can propagate along the $\mathbf{s}$ direction in the anisotropic crystal. It can be done finding the intersection

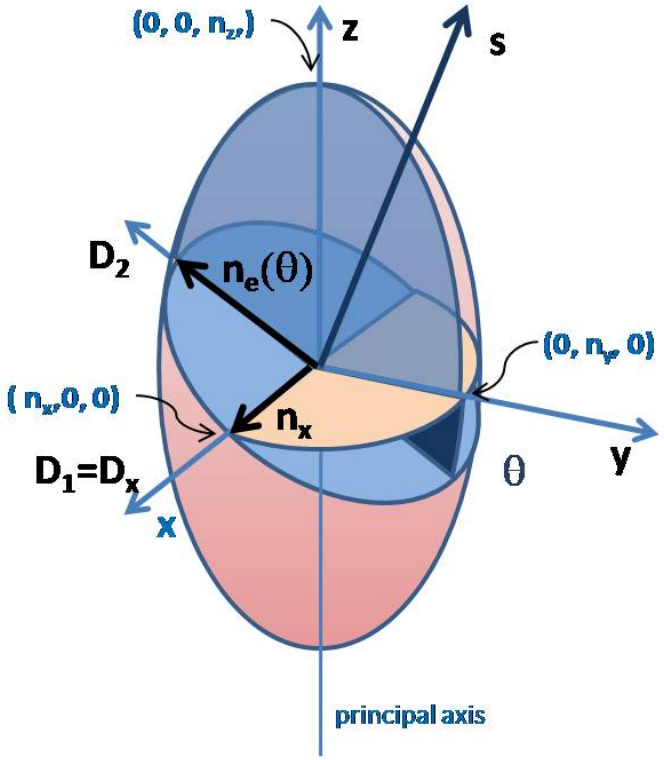

Figure 2.7: Index Ellipsoid. The intersection between the plane orthogonal to the propagation direction **s** and the index ellipsoid is an ellipse with the axes parallel to the polarization of the two allowed independent waves that can propagate in the crystal. The ellipse semi-axes length is equal to refractive index feels by those waves, n_1 and n_2, respectively. The ellipsoid principal axes correspond to the only direction in the crystal along which the electric field, **E**, is parallel to the displacement vector **D**.

between the index ellipsoid and the plane orthogonal to the propagation direction **s**, as shown in figure 2.7. This intersection is an ellipse with the axes parallel to the polarization of the two allowed independent waves that can propagate in the crystal. The ellipse semi-axes length is equal to refractive index feels by those waves, n_1 and n_2, respectively.

Obviously to quantify the refractive index we have to solve mathematically the problem, that means, we have to find the intersection between the ellipsoid and the surface normal to the propagation direction **s**. This is equivalent to solve the equation (2.55) [26], [27].

The wave propagating along the principal axis of the index ellipsoid hold

the electric field parallel to the displacement vector.

Chapter 3

Basic Physical Effects in Passive Optoelectronic Devices

In this chapter we would like to give a brief overview on the main physic effects involved in the most common optoelectronic devices.

We start with the basic phenomenon which allows to realize one of the widely used element, the distributed reflector, or more commonly known as *Bragg reflector*. It is built by means of periodic perturbations inside the core waveguides like periodic corrugations of the guiding film/cover interface or periodic distribution of refractive index, both equivalent to a periodic perturbation of the effective refractive index in the section of the waveguide. The periodicity of the perturbation selects a specific wavelength, tuned to the period, which, like in a multi-layer, can be repetitively reflected so that by interference a reflected intense wave is made. It is used, thus, to filter a wavelength; in the integrated laser to realize the feedback which allows to select and amplify the laser wavelength; to realize intensity modulators, temperature and strain sensor in optical fibers and other kind of devices.

The physics of the Bragg reflector is based on the coupling between two contro-directional modes in the waveguide. To understand how it can happen, we resort to the *Coupled Mode Theory* (section 3.1), which is an elegant, analytic method to explain the coupling modes in the waveguides. Nevertheless, since our work is to design the optoelectronic devices, the theory which we present in these first chapters has only the goal to shown and better understand the practices tools which we use and have used, we present in the section 3.2 a power as much elegant method, let alone widely used, to analyze and especially to numerically simulate (and thus to predict) the op-

tical response of the distributed reflectors: the Impedance-Matching Matrix Method [28, 29, 30, 31, 32, 33].

The chapter then continues with a short overview on the main physic effects which induce a refractive index variation in the semiconductor materials. By means of this mechanism, in fact, a lot of functionalities in the optoelectronic device are obtained, first between these the signal intensity modulation, which play a relevant role in the communication systems. The most effects are induced by an suitable electric field is applied to a semiconductor. They can be differentiated in two main type of effects. The first one is related directly to electric field (*electro-optic effect*), while the others are related to the change of the free carriers concentration (*carriers induced effects*). At least we conclude with a brief reminding on the *thermooptic effect* which is the change in the refractive index due to the change of temperature, exploited in the temperature sensors and to test the stability of the devices working point.

3.1 Coupling between modes: The Coupled Mode Theory

In the section 2.3 we have seen that a waveguide can supports, in general, several modes. Usually this mode are not coupled. In mathematic language, since the set of the waveguide modes constitutes a wave equation solution base, they are mutually orthogonal and independent, and each of them is solution of the wave equation. For example, the electric field of the $m-th$ TE modes satisfy

$$\left[\frac{\partial^2}{\partial x^2} + \omega^2 \mu \epsilon(\mathbf{r})\right] \mathcal{E}_y^{(m)}(\mathbf{r}) = \beta_m^2 \mathcal{E}_y^{(m)}. \tag{3.1}$$

where, we remember, ω is the light angular frequency, μ the magnetic permeability, ϵ_0 the dielectric constant, β_m the propagation constant of the *m-th* mode, or, in others words, the eigenvalue correspondent to the *m-th* modes.

Nevertheless if the waveguide structure is suitably perturbed, the coupling between two different mode can occurs. Depending on the perturbation kind it is possible to couple a TE mode to a TM mode, like in electrooptic or acustooptic effect [26, 34, 35], or a forward wave to a backward wave by means of a corrugation between two dielectric interface of the waveguide [36]. These mechanism are exploited in a lot of devices like reflectors, filters,

modulators and so on.

To understand how it can happens, let us consider a perturbation of the electric permittivity $\epsilon(\mathbf{r})$

$$\epsilon(\mathbf{r}) = \epsilon_0 \left[n^2(\mathbf{r}) + \Delta n^2(\mathbf{r} \right] \tag{3.2}$$

so that for a generic TE polarized field propagating inside the waveguide, the wave equation can be write as

$$\left[\nabla^2 - \mu\epsilon(\mathbf{r}) \frac{\partial^2}{\partial t^2} \right] E_y(\mathbf{r}, t) = \mu\epsilon_0 \frac{\partial^2}{\partial t^2} \Delta n^2(\mathbf{r}) E_y(\mathbf{r}, t), \tag{3.3}$$

where the summation is for $m = \pm|m|$, seeing that there are a forward and a backward term correspondent to the same amplitude $\mathcal{E}_y^m$. Since the field can be expressed as linear combination of the waveguide TE modes

$$E_y(\mathbf{r}, t) = \frac{1}{2} \sum_m A_m(z) \mathcal{E}_y^{(m)}(x) e^{i(\omega t - \beta_m z)} + c.c., \tag{3.4}$$

the (3.3) leads to

$$\begin{aligned} e^{i\omega t} \sum_m \left[\frac{A_m}{2} \left(-\beta_m^2 + \frac{\partial^2}{\partial x^2} + \omega^2 \mu\epsilon(\mathbf{r}) \right) \mathcal{E}_y^{(m)} e^{-i\beta_m z} \right] \\ + e^{i\omega t} \sum_m \left[\frac{1}{2} \left(-2i\beta_m \frac{dA_m}{dz} + \frac{d^2 A_m}{dz^2} \right) \mathcal{E}_y^{(m)} e^{-i\beta_m z} \right] + c.c. \\ = \mu \frac{\partial^2}{\partial t^2} \left(\epsilon_0 \Delta n^2(\mathbf{r}) E_y(\mathbf{r}, t) \right). \end{aligned} \tag{3.5}$$

By (3.1) we deduce that the first line in the previous equation vanish; assuming than *slow variation* along the propagaton axis z, so that is

$$\left| \frac{d^2 A_m}{dz^2} \right| \ll \beta_m \left| \frac{dA_m}{dz} \right|, \tag{3.6}$$

and projecting the (3.5) on the $s-th$ autosite, we arrive to

$$\begin{aligned} \frac{A_s^+}{dz} e^{i(\omega t + \beta_s z)} - \frac{A_s^-}{dz} e^{i(\omega t - \beta_s z)} - c.c. \\ = \frac{i\omega\epsilon_0}{2} \int_{-\infty}^{\infty} \Delta n^2(x, z) E_y(x, z, t) \mathcal{E}_y^s(x) dx. \end{aligned} \tag{3.7}$$

In the right side of the last equation there is the *coupling term*. It is like a source that can drive the terms in the left side. In order that this happens, it is necessary that the source have the same frequency of the waves and

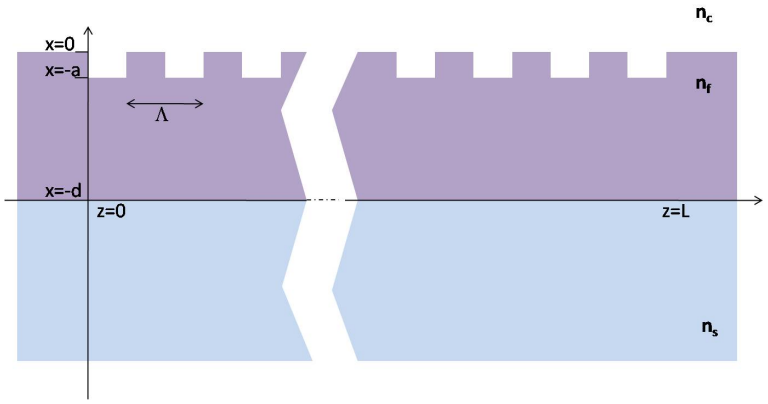

Figure 3.1: Periodic perturbation of the waveguide core.

the same phase, so that the interaction does not vanish after a long time (compared to their period). The first condition is satisfied, since $\Delta n^2(x,z)$ does not depend on the time t. To better understand the second condition, let we expand again the field E_y in modes superposition (3.4):

$$\frac{i\omega\epsilon_0}{2}\sum_{m>0}\left[A_m^+\int_{-\infty}^{\infty}\Delta n^2(x,z)e^{i(\omega t-\beta_m z)}\mathcal{E}_y^{(m)}\mathcal{E}_y^(s)(x)dx+c.c.\right] + \frac{i\omega\epsilon_0}{2}\sum_{m>0}\left[A_m^-\int_{-\infty}^{\infty}\Delta n^2(x,z)e^{i(\omega t+\beta_m z)}\mathcal{E}_y^{(m)}\mathcal{E}_y^(s)(x)dx+c.c.\right], \quad (3.8)$$

(in the summation we have made the modes traveling along the z direction and the modes traveling along the $-z$ direction explicit). It is now clear that if we want excite, for example, the forward wave $A_s^{(+)}$, at left there must be at least one term with phase factor equal to $exp[i(\omega t-\beta_s)]$. In this manner the equation (3.7) can be simplified keeping only these terms on the right.

3.1.1 The Coupled Mode Equations for Periodic Waveguides

Let us consider now a periodic perturbation, with period Λ, of the waveguide guiding film, like that one shown in the figure 3.1. In this case we can expand the perturbation $\Delta n^2(x,z)$ as a Fourier Serie

$$\Delta n^2(x,z)=\Delta n^2(x)\sum_{-\infty}^{\infty}a_q\exp iq\frac{2\pi}{\Lambda}z, \quad (3.9)$$

so that, if we want to couple the backward modes A_s^- to the forward mode A_s^+, the previous considerations suggest that must be

$$\frac{2l\pi}{\Lambda} - \beta_s = \beta_s \tag{3.10}$$

with the result that the equation (3.7) is reduced to a set of two *coupled equations* that involve only the two modes A_s^- and A_s^+:

$$\begin{aligned} \frac{dA_s^-}{dz} &= \kappa A_s^+ e^{-i2(\Delta\beta_s)z} \\ \frac{dA_s^+}{dz} &= \kappa^* A_s^- e^{i2(\Delta\beta_s)z}, \end{aligned} \tag{3.11}$$

in which

$$\Delta\beta = \beta_s - \frac{l\pi}{\Lambda} \equiv \beta_s - \beta_0 \tag{3.12}$$

and the *coupling coefficient*

$$\kappa = \frac{i\omega\epsilon_0}{2} \int_{-\infty}^{\infty} \Delta n^2(x) a_l \left[\mathcal{E}_y^{(s)}(x)\right]^2 dx \tag{3.13}$$

has been defined.

If the periodic region inside the waveguide has length equal to L, the solution of the system 3.1.3 for the initial condition $A^-(L) = 0$ (correspondent to have not reflected wave at the output of the periodic region), putting

$$S = \sqrt{\kappa^2 - \Delta\beta^2},$$

is

$$\begin{aligned} A^-(z) &= A^+(0) \frac{\sinh\left[S(z-L)\right]}{-\Delta\beta \sinh SL + iS\cosh SL} |\kappa| e^{-i\Delta\beta_0 z} \\ A^+(z) &= A^+(0) \frac{\Delta\beta \sinh\left[S(z-L)\right] + iS\cosh\left[S(z-L)\right]}{-\Delta\beta \sinh SL + iS\cosh SL} e^{i\Delta\beta_0 z}, \end{aligned} \tag{3.14}$$

reduced to

$$\begin{aligned} A^-(z) &= A^+(0) \frac{\sinh\left[|\kappa|(z-L)\right]}{\cosh|\kappa|L} \frac{\kappa}{|\kappa|} \\ A^+(z) &= A^+(0) \frac{\cosh\left[|\kappa|(z-L)\right]}{\cosh|\kappa|L} \end{aligned} \tag{3.15}$$

in the case of the phase-matching conditions, $\Delta\beta = 0$.

In the figure 3.2 the trend of the power of the backward mode, $|A^-(z)|^2$ (red line), and of the forward mode, $|A^+(z)|^2$ (yellow line), along the corrugated waveguide in the phase-matching condition is shown. There is a power

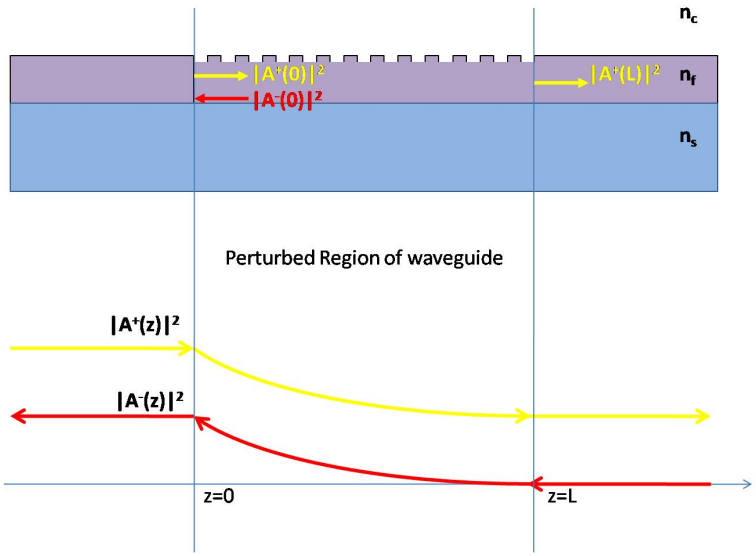

Figure 3.2: Trend of the power of the backward mode, $|A^-(z)|^2$ (red line), and of the forward mode, $|A^+(z)|^2$ (yellow line), along a corrugated waveguide in phase-matching condition. There is a power exchange between the two mode inside the perturbed region: the forward wave lets its power to the backward wave, so that increases the reflectance at the beginning of the corrugation.

exchange between the two modes inside the perturbed region: the forward wave lets its power to the backward wave, so that increases the reflectance at the beginning of the corrugation. If the arguments of the hyperbolic cosine and hyperbolic sine function in the (3.1.1) are large enough, this exchange appears as an exponentially decay of the forward wave, correspondent to an exponentially increase of the backward wave.

From the (3.1.1) we can derive the *reflectance*, R, and *transmittance*, T, of the the corrugated region

$$R \equiv \left|\frac{A^-(0)}{A^+(0)}\right| = \left|\frac{\kappa \sinh(SL)}{-\Delta\beta \sinh SL + iS \cosh SL}\right|^2$$

$$T \equiv \left|\frac{A^+(L)}{A^+(0)}\right| = \left|\frac{Se^i\Delta\beta}{-\Delta\beta \sinh SL + iS \cosh SL}\right|^2, \tag{3.16}$$

and the z-dependent part of the propagating waves

$$\beta' = \beta_0 \pm iS = \frac{l\pi}{\Lambda} \pm \sqrt{\kappa^2 - [\beta(\omega) - \beta_0]}. \tag{3.17}$$

We note that:

1. it is verified the energy conservation, since it is

$$T + R = 1; \tag{3.18}$$

2. the reflectance, R, increases when $\Delta\beta$ vanishes, while obviously, the transmittance, T, reaches the unity;

3. since the mode eigenvalue β depend on the light frequency, ω, the mismatch too depend on the frequency, so that there is a frequency interval in which β' has an imaginary part, since $\Delta\beta(\omega) < \kappa$.

About the last observation, we have to say that the individuated range is the so-called *forbidden region*, since if this happens the transmittance has an evanescent behavior like in figure 3.2, which means that the energy impinging the perturbed region of the waveguide cannot be transmitted, but only reflected. This region is like the *band-gap* in the periodic potential inside the semiconductor crystal. It is nowadays known that periodic structures (the so-called *photonic-crystal*) originate transmittance band-gap and the periodic perturbed waveguides are example of 1D-photonic-crystal. Furthermore we must stress that the band-gap exists for each value of mode-order

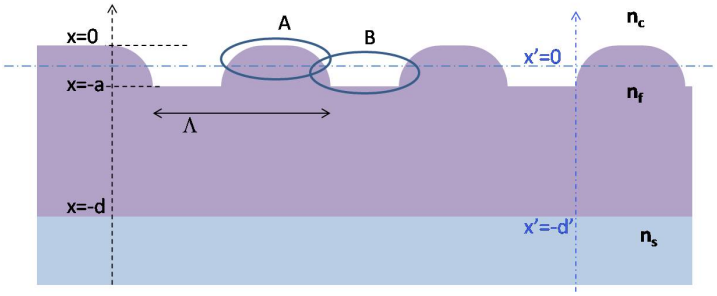

Figure 3.3: Illustration of the correction to the coupling coefficient calcultion [37]. The interface between the core and the cover is taken so that the perturbation is equitably distributed between the core and the cover, that means the area named A must be equal to the area named B.

$l = 0, 1, 2, 3, ...$, and it is centered in ω_0 such that $\beta(\omega_{0l}) = l\pi/\Lambda$, called *Bragg frequency*, in accordance with what previous said. Exception is for the values for which $\kappa = 0$. Developing the perturbed propagation constant β' near the Bragg frequency ω_0

$$\beta' \approx \frac{l\pi}{\Lambda} \pm l\sqrt{\kappa^2 . \left(\frac{n_{eff}}{c}\right)^2 (\omega - \omega_0)} \tag{3.19}$$

we see that

$$\beta' \xrightarrow{\omega \longrightarrow \omega_0} \beta_0 = \frac{l\pi}{\Lambda}. \tag{3.20}$$

which mens that the Bragg frequency ω is the frequency for which the perturbed propagation β' constant is equal to the unperturbed propagation constant β.

We can conclude that a periodically perturbed waveguide acts as a reflector with the reflectance maximum at the Bragg frequency.

3.1.2 The Coupling Coefficient

Let us return on the expression (3.13) of the coupling coefficient, that we rewrite

$$\kappa = \frac{i\omega\epsilon_0}{2} \int_{-\infty}^{\infty} \Delta n^2(x) a_l \left[\mathcal{E}_y^{(s)}(x)\right]^2 dx. \tag{3.21}$$

How we said at the begin of this section, from the previous expression is clear that the coupling coefficient depend on the perturbation, $\Delta n(x)^2$, and, obviously, on the solutions $\mathcal{E}_y^{(s)}(x)$ of the unperturbed structure that we are considering. As consequence, to compute κ and then to solve the equations (3.1.3), we must give a shape at the perturbation $\Delta n(x)^2$.

At this point we note that since the unperturbed structure is a three-layer waveguide, the classical perturbative approach is thus to replace in the (3.21) the solutions (2.32). But a problem rises. In fact the first studies [38, 39, 40] included whole the perturbation in the guiding layer . Nevertheless, as observed in [41], this can lead to inaccurate excessively high coupling coefficient. Those authors demonstrated a better agreement using a four-layer unperturbed solutions $\mathcal{E}_y^{(s)}(x)$. Fortunately, without resort to the more complicate four-layer structure, in [37] was shown that the three-layer unperturbed solutions can be used with good results, taking care to choose an effective height of the guiding film, so that half of the perturbed region is included in the guiding layer, and the other half in the adjacent layer. To be more precise, referring to figure 3.3, taking the same system of cartesian axes of the figure 3.1, the origin of the x axis (correspondent to the interface between the guiding layer and the cover of the unperturbed guide) must be translated below the top of the perturbed region so that the area of this region above the zero, A, is equal to the area below the zero, B. As consequence in the expression (2.32) the real thickness of the guiding layer must be replaced with the effective thickness d'

$$\mathcal{E}_y(x) = \begin{cases} \mathcal{B}_c e^{\gamma_c x'} & x \geq 0 \\ \mathcal{B}_c \left(\cos \gamma_f x - \dfrac{\gamma_c}{\gamma_f} \sin \gamma_f x \right) & -d' < x < 0 \\ \mathcal{B}_c \left(\cos \kappa_f d' + \dfrac{\gamma_c}{\gamma_f} \sin \gamma_f x \right) e^{\gamma_s (x+d')} & x \leq -d', \end{cases} \tag{3.22}$$

with γ_c, γ_f and γ_s given by the (2.18). The constant $\mathcal{B}$, as far said, can be determined imposing the mode normalization (which physically correspond to the energy normalization)

$$\frac{\beta}{2\omega\mu} \int_{-\infty}^{\infty} [\mathcal{E}(x)]^2 \, |dx = 1. \tag{3.23}$$

We remand to [37] for the details of the computations, and note only that in the more general case if $w_i(x)$ are the function which describe the

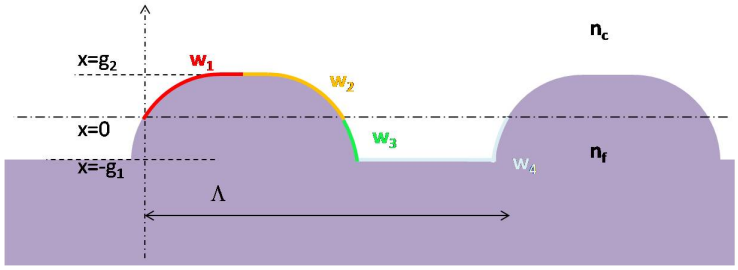

Figure 3.4: Details of the illustration of the correction to the coupling coefficient calcultion [37]. The function $w_i(x)$ define the corrugation profile in the calculation of the coupling coefficient (formulas 3.24 and (3.25)).

perturbation profile (see figure 3.4), the Fourier series (3.9) becomes

if $x > 0$

$$\Delta n^2(x,z) = \left(n_c^2 - n_f^2\right) \frac{w_2(x) - w_1(x)}{\Lambda}$$

$$- \left(n_c^2 - n_f^2\right) \left[\frac{i}{2\pi} \sum_{m=-\infty}^{+\infty} \left(e^{i\frac{2\pi m}{\Lambda} w_2(x)} - e^{i\frac{2\pi m}{\Lambda} w_1(x)} \right) e^{-i\frac{2m\pi}{\Lambda} z} \right] \quad (3.24)$$

in the region named A in the figure 3.3, while

if $x < 0$

$$\Delta n^2(x,z) = \left(n_f^2 - n_c^2\right) \frac{w_4(x) - w_3(x)}{\Lambda}$$

$$- \left(n_f^2 - n_c^2\right) \left[\frac{i}{2\pi} \sum_{m=-\infty}^{+\infty} \left(e^{i\frac{2\pi m}{\Lambda} w_4(x)} - e^{i\frac{2\pi m}{\Lambda} w_3(x)} \right) e^{-i\frac{2m\pi}{\Lambda} z} \right] \quad (3.25)$$

corresponding to the region named B in figure 3.3.

3.1.3 Waveguides with losses

The equation (3.7) describe the coupling between a back-propagating wave and a forward-propagating wave across a periodically perturbed waveguide when any losses and any gain is present in the waveguide medium. The losses or gain in a medium can be described by means of macroscopic coefficient, γ, such that the propagation inside the medium of a wave suffers of an exponential decay, in the case of absorbtion, or an exponential growth in the

case of gain. We have take into account this variation of the intensity into the coupled mode equations (3.1.3), so that they becomes [36]

$$\begin{aligned}\frac{dA_s^-}{dz} &= \kappa A_s^+ e^{-2i(i\Delta\beta_s+i\gamma)z} \\ \frac{dA_s^+}{dz} &= \kappa^* A_s^- e^{2(i\Delta\beta_s+i\gamma)z}.\end{aligned} \tag{3.26}$$

The previous equations are similar to the (3.1.3) with $\Delta\beta$ replaced by $\Delta\beta_s + i\gamma$. Taking into account this substitution, we can rewrite the reflectance and the transmittance of the perturbed waveguide as

$$\begin{aligned}R &= \left|\frac{\kappa \sinh(SL)}{(\gamma - i\Delta\beta)\sinh SL + S\cosh SL}\right|^2 \\ T &= \left|\frac{Se^{\gamma - i\Delta\beta}}{(\gamma - i\Delta\beta_s)\sinh SL + S\cosh SL}\right|^2,\end{aligned} \tag{3.27}$$

where now is

$$S^2 = |\kappa|^2 + (\gamma - i\Delta\beta)^2 \tag{3.28}$$

Since in this case S is complex, there is a significant difference with the case of passive waveguide, previous examined. If $\gamma < 0$, like in the case of losses, we have a reflectance and transmittance decrease. Otherwise, the more interesting case, if we are in presence of gain, so that is $\gamma > 0$, the reflectance and transmittance can be infinite if

$$(\gamma - i\Delta\beta)\sinh SL + S\cosh SL = 0.$$

This condition corresponds to a threshold condition to have an reflected wave and a transmitted wave whiteout input field. Thus the periodic waveguide acts as an optical oscillator. This is the basic phenomenon in the so called *Distributed Feedback Laser*, where the periodically perturbation, that is the mede Bragg Grating, constitutes the feedback cavity, which amplifies the gain and selects the oscillation mode.

3.2 Coupling between modes: Impedance-Matching Matrix Method

The coupled mode method is an elegant theory to analyze and to understand the periodic perturbation in the waveguides, provided that the perturbation is small, which means that the depth of the etching on the waveguide must be small compared to the guiding film thickness. Although it has been to nonuniform grating [42, 43] and to deep grating (linear and non linear) [44], in these cases it becomes very complicated and often too much laborious to be applied especially to be implemented in numerical codes to design devices. A powerful tool and as much elegant is the Impedance-Matching Matrix Method, which is a combined Effective-Index/Impedance-Matching matrix technique [**?**], proposed the first time by Wang [28] and developed subsequently by Basu and Ballantyne [29], Bjork and Nilsson [30] and Verly *et al.* [31, 32].

This method divides the corrugated waveguide into a large number of thin sections. Each section is treated as a three-layer waveguide, and the standard analytic method is used to compute the propagating modes that are supported by this guide. A 2 x 2 transfer matrix for the section is then derived by matching the tangential E and H fields, correspondent to these modes, at the interfaces between the sections. Finally, the transfer matrix for the complete structure is obtained by multiplying together the individual transfer matrices.

Winick [33] given an excellent exposition of the method, together with a comparison whit tha coupled-mode theory. In the follow, we refer to his paper.

Consider a planar waveguide as shown in figure 3.5, where the film between the cover and substrate has a periodically spacial distribution of refractive index. Let is n_c the refractive index of cover layer; n_s the refractive index of substrate layer and n_f that one of film layer, where is $n_c > n_s > n_f$ We can consider the waveguide as a collection of slabs, numbered 0 through $2N+1$, of length w_k and with effective refractive index N_k, computed solving the stationary wave equations in the three-layer guide [26].

Focusing the attention on waves propagating along the waveguide axis, z, suppose that the periodic grating couples only two controdirectional TE wave modes, we can write the electric field in kth slab as

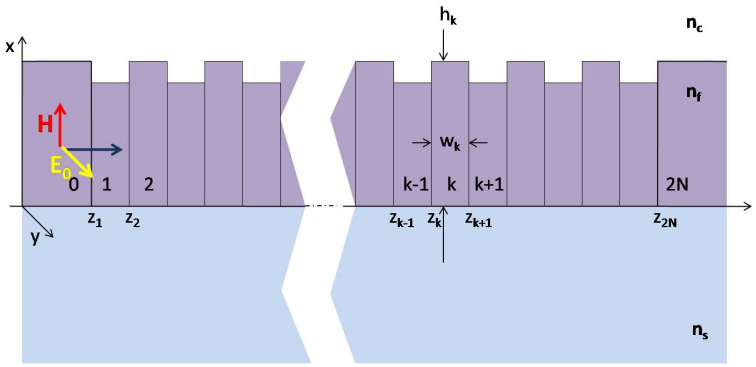

Figure 3.5: In the *Impedance-Matching Matrix Method* the periodically perturbed structure is subdivided in a sequence of layer, each characterized by an constant effective index.

$$E_k(x,y,z) = E_{Fk}(x,y,z) + E_{Bk}(x,y,z), \tag{3.29}$$

with

$$E_{Fk}(x,y,z) = AE_{yk}(x,y)e^{-i\beta_k z} \tag{3.30}$$
$$E_{Bk}(x,y,z) = BE_{yk}(x,y)e^{-i\beta_k z}, \tag{3.31}$$

being

$$\beta_k = \frac{2\pi}{\lambda}N_k \tag{3.32}$$

the propagation constant.

From Maxwell's equations we derive the x-component of magnetic field

$$H_{Fk}(x,y,z) = -\frac{\beta_k}{\omega\mu_o}E_{Fk}(x,y,z)$$
$$H_{Bk}(x,y,z) = \frac{\beta_k}{\omega\mu_o}E_{Bk}(x,y,z).$$

Named z_k the position of the boundary between the *(k-1)-th* and *k-th* slabs, we have the follow relation between the field just at left and which one just at right of the *k-th* boundary

$$E_{Fk-1}(x,y,z_k^-) + E_{Bk-1}(x,y,z_k^-) = E_{Fk}(x,y,z_k^+) + E_{Bk}(x,y,z_k^+)$$
$$\frac{N_{k-1}}{Z_o}\left[E_{Fk-1}(x,y,z_k^-) + E_{Bk-1}(x,y,z_k^-)\right] = \frac{N_k}{Z_o}\left[E_{Fk}(x,y,z_k^+) + E_{Bk}(x,y,z_k^+)\right],$$

where $\frac{N_k}{Z_o} = \frac{\beta_k}{\omega\mu_o}$ and $Z_o = \sqrt{\frac{\mu_o}{\varepsilon_o}}$ is the vacuum impedance.
Defining

$$\mathcal{V}_k = \frac{1}{Z_o}\begin{bmatrix} 1 & 1 \\ -N_k & N_k \end{bmatrix},$$

we can write in matrix form the previous equations

$$\begin{bmatrix} E_{Fk}(x,y,z_k^-) \\ E_{Bk}(x,y,z_k^-) \end{bmatrix} = \mathcal{V}_k^{-1}\mathcal{V}_k \begin{bmatrix} E_{Fk}(x,y,z_k^+) \\ E_{Bk}(x,y,z_k^+) \end{bmatrix}, \tag{3.33}$$

so that $\mathcal{V}_k^{-1}\mathcal{V}_k$ represent the propagation matrix across the kth boundary.

From (3.30) and (3.31), considering possible gain or absorbtion, g_k, in the medium, the propagation across the kth slab, is

$$\begin{bmatrix} E_{Fk}(x,y,z_k^+) \\ E_{Bk}(x,y,z_k^+) \end{bmatrix} = \mathcal{U}_k \begin{bmatrix} E_{Fk}(x,y,z_{k+1}^-) \\ E_{Bk}(x,y,z_{k+1}^-) \end{bmatrix}$$

where,

$$\mathcal{U}_k = \begin{bmatrix} e^{\Lambda_k(i\beta_k - g_k)} & 0 \\ 0 & e^{-\Lambda_k(i\beta_k - g_k)} \end{bmatrix}.$$

Therefore the *transfer matrix* of *k-th* slab results to be $\mathcal{M}_k = \mathcal{V}_k^{-1}\mathcal{V}_k\mathcal{U}_k$, that is, in explicit form

$$\mathcal{M}_k = \begin{bmatrix} \left(1 - \frac{\Delta\beta_k}{2N_{k-1}}\right) e^{\Lambda_k(i\beta_k - g_k)} & \left(\frac{\Delta\beta_k}{2N_{k-1}}\right) e^{-\Lambda_k(i\beta_k - g_k)} \\ \left(\frac{\Delta\beta_k}{2N_{k-1}}\right) e^{\Lambda_k(i\beta_k - g_k)} & \left(1 - \frac{\Delta\beta_k}{2N_{k-1}}\right) e^{-\Lambda_k(i\beta_k - g_k)} \end{bmatrix} \tag{3.34}$$

with $\Delta\beta_k = \beta_{k-1} - \beta_k$.

The transfer matrix of one period is $\mathcal{M}_k\mathcal{M}_{k+1}$, so that we have

$$\begin{bmatrix} E_{Fk-1}(x,y,z_k^-) \\ E_{Bk-1}(x,y,z_k^-) \end{bmatrix} = \mathcal{M}_k\mathcal{M}_{k+1} \begin{bmatrix} E_{Fk}(x,y,z_{k+2}^-) \\ E_{Bk}(x,y,z_{k+2}^-) \end{bmatrix}, \tag{3.35}$$

while for the whole grating, keeping in mind we want the relation between

the field just at beginning of the grating (that is in z_1^-) and that one just at end (that is in z_{2N}^+), from (3.33) and (3.35) we have

$$\begin{bmatrix} E_{F0}(x,y,z_1^-) \\ E_{B0}(x,y,z_{1k}^-) \end{bmatrix} = M_G \begin{bmatrix} E_{F2N}(x,y,z_{2N+1}^+) \\ E_{B2N}(x,y,z_{2N+1}^+) \end{bmatrix} \tag{3.36}$$

where the transfer matrix of grating is

$$M_G = \left(\prod_{k=1}^{2N} \mathcal{M}_k \mathcal{M}_{k+1} \right) \mathcal{V}_{2N+1}^{-1} \mathcal{V}_{2N+1}.$$

From the (3.36), if we set $\left(E_{F2N}(x,y,z_{2N+1}^+), E_{B2N}(x,y,z_{2N+1}^+)\right) = (1,0)$, we can compute the grating reflection coefficient

$$r(\lambda) = \frac{E_{F0}(x,y,z_1^-)}{E_{B0}(x,y,z_{1k}^-)},$$

and therefore the grating reflectivity.

3.2.1 Reflectivity and Transmittivity and Characteristic Matrix eigenvalues

In the [33] an explicit expression of the total period matrix $M_k = \mathcal{M}_{\|}\mathcal{M}_{\|+\infty}$ is given and the reflectance and the transmittance in the case of small perturbation near the Bragg condition is computed to show that the method agrees to the coupled-mode theory.

Without report here those computation we report instead an general analysis of the transfer matrix $\mathcal{M}_{\mathcal{G}}$, which can help to easily understand the grating behavior (we remaind that we are considering periodic perturbation).

First of all we rewrite the grating matrix (we remaind that we are considering periodic perturbation) M_G as a general ABCD matrix,

$$M_T = \begin{bmatrix} A_N & B_N \\ C_N & D_N \end{bmatrix}. \tag{3.37}$$

so that, after some calculation [45], we can derive a general expression for

the *reflectance* and the *transmittance*

$$R = \left| \frac{\left(A_N + \frac{n_o}{Z_0} B_N\right) - \frac{Z_0}{n_i}\left(C_N + \frac{n_o}{Z_0} D_N\right)}{\left(A_N + \frac{n_o}{Z_0} B_N\right) + \frac{Z_0}{n_i}\left(C_N + \frac{n_o}{Z_0} D_N\right)} \right|^2 \tag{3.38}$$

$$T = \frac{n_o}{n_i} \left| \frac{2}{\left(A_N + \frac{n_o}{Z_0} B_N\right) + \frac{Z_0}{n_i}\left(C_N + \frac{n_o}{Z_0} D_N\right)} \right|^2 \tag{3.39}$$

being n_o and n_i the refractive index at the input and at the output of the perturbation.

To describe the perturbation behavior, we observe that the period transfer matrix $M_k = \mathcal{M}_k \mathcal{M}_{k+1}$, as all the matrix which represent an optical system, is an 2x2 unitary matrix, so that we can diagonalize it. Named u_1 and u_2 the eigenvectors and η_1 and η_2 the eigenvalues, we can write

$$M_k = \begin{bmatrix} A & B \\ C & D \end{bmatrix} [u_1 \quad u_2] \begin{bmatrix} \eta_1 & 0 \\ 0 & \eta_2 \end{bmatrix} [u_1 \quad u_2]^{-1}$$

and, since must be $\eta_1 \cdot \eta_2 = 1$,

$$\eta_1 = e^{\gamma z + i(2m-1)\pi} \tag{3.40}$$

$$\eta_2 = e^{-\gamma z + i(2m-1)\pi} \tag{3.41}$$

with m integer correspondent to the order of the propagating mode. The (3.2.1) suggests that from the matrix trace derives the following relation

$$\frac{A+B}{2} = \cosh \gamma z \tag{3.42}$$

so that the following cases are possible:

1. if $-1 < \frac{A+B}{2} < 1$, then γ is real so that both the modes are in *cut-off*, since they have a decay along the z axis.

2. if $\frac{A+B}{2}$, then γ is imaginary and the correspondent mode can propagate.

We conclude that there exist a frequency range in which the propagation of both the forward and backward mode is allowed, while outside is forbidden. It is possible to show that the center of this interval is the Bragg frequency.

3.2.2 Transfert Matrix of the Perfectly Periodic Grating

If the perturbation is perfectly periodic (that means $\Lambda_k = \Lambda_{k+2n}$, with $n = (1, 2, ..., N)$, is $M_k = M_{k+n}$, and the *transfer matrix* of the whole grating becomes

$$M_G = M_T^N = \begin{bmatrix} A & B \\ C & D \end{bmatrix} = [u_1 \quad u_2] \begin{bmatrix} \eta_1^N & 0 \\ 0 & \eta_2^N \end{bmatrix} [u_1 \quad u_2]^{-1} . \tag{3.43}$$

The previous expression of the transfer matrix is particularly useful in the numeric iterative code, since it allow to reduce the computational time.

3.2.3 TM mode

We conclude this section on the combined effective index/impedance matching method observing that it does not account for the boundary conditions at grating-cover interface. Thus, though in the case of TE mode this is not a problem, since the **E** and **H** fields are continuous across this interface, in the case of the TM mode, to consider the conditions at this interface [32], we must modify the matrix $\mathcal{M}_k$, reducing the term $\frac{\Delta N_k}{2N_{k-1}}$ by the factor [33]:

$$\frac{N_{av}/n_f - N_{av}/nc + 1}{N_{av}/n_f + N_{av}/nc - 1},$$

where

$$N_{av} = \frac{\lambda}{2\pi} (\beta_k + \beta_{k+1}) \qquad\qquad k = 1, 2, ...$$

3.3 The Electrooptic Effect

We have seen in the section 2.5 that in the anisotropic medium the refractive index depend on direction of propagation of the light. The crystal symmetries allow to determine same main direction (*principal axes*) along which the refractive index is determined, and from which we can easily know the value of the refractive index along other arbitrary direction by mean of the so called *index ellipsoid* [26]. The effect of an suitable electric field in non linear medium is to change this principal axes, in particularly we can observe a direction-dependent effect at first order, known as *linear electrooptic effect* or *Pockels effect*, which rotates and changes the length of these axes, and a quadratic effect depending on the square of the applied external electric

field, known as *Kerr effect*, which induces only a change of the length of the principal axis.

3.3.1 The linear electro-optic effect

To explain the electro-optic effect, we will make use of the index ellipsoid, which, as said, fully describes the propagation inside a crystal. Therefore it is advantageous to express the effects of an electric field on the propagation in terms of the change of the index ellipsoid coefficients.

Following [26], we write the equation of the index ellipsoid in the presence of an electric field as

$$\alpha_1 x^2 + \alpha_2 y^2 + \alpha_3 z^2 + 2\alpha_4 yz + 2\alpha_5 xz + 2\alpha_6 xy = 1, \tag{3.44}$$

so that, if we chose the x, y and z axes parallel to the principal axes of the crystal and named n_1, n_2 and n_3 respectively the refractive indices along these axes, when the applied field is zero, in order to have the (2.65), must be

$$\alpha_i = \begin{cases} \dfrac{1}{n_i^2} & \text{for } i = 1, 2, 3 \\ 0 & \text{for } i = 4, 5, 6. \end{cases} \tag{3.45}$$

When an electric field $\mathbf{E} = (E_x, E_y, E_z)$ with an arbitrary "low-frequency", is present, at first order, the change of the index coefficients can be written as

$$\begin{bmatrix} \Delta\alpha_1 \\ \Delta\alpha_2 \\ \Delta\alpha_3 \\ \Delta\alpha_4 \\ \Delta\alpha_5 \\ \Delta\alpha_6 \end{bmatrix} = \begin{bmatrix} r_{11} & r_{12} & r_{13} \\ r_{21} & r_{22} & r_{23} \\ r_{21} & r_{32} & r_{33} \\ r_{41} & r_{42} & r_{43} \\ r_{51} & r_{52} & r_{53} \\ r_{61} & r_{62} & r_{63} \end{bmatrix} \begin{bmatrix} E_x \\ E_y \\ E_z \end{bmatrix}, \tag{3.46}$$

where the $\mathbf{r}$ tensor is called *electro-optic tensor* of the material. From the crystal symmetries we can deduce which of the 18 r_{ij} coefficients are zero, but not their magnitude, for example, the centrosymmetric crystals show $r_{ij} = 0\ \forall i, j$, while the cubic crystals with a $\bar{4}3$ symmetries, like GaAs, InP, InGaAsP, have all the element zero except r_{41}, r_{52} and r_{63}, which are equal.

In the following we will illustrate a particular case of a cubic crystals with a $\bar{4}3$ symmetries,

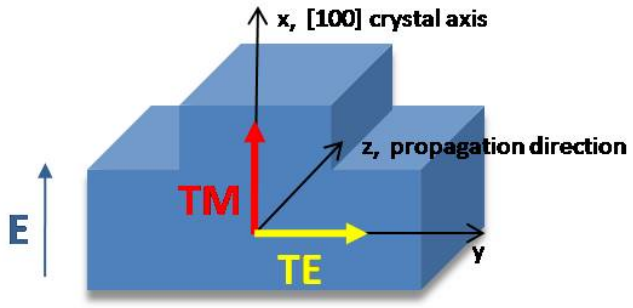

Figure 3.6: Rib waveguide grown on on (100) substrate of a cubic crystals with a $\bar{4}3$ symmetries, and an electric field along the [100] direction, coincident with the x axis.

Pockels effect for cubic crystals with a $\bar{4}3$ symmetries

Let us consider an optoelectronic device built on a wafer grown on (100) substrate of a cubic crystals with a $\bar{4}3$ symmetries, and an electric field along the [100] direction (the x axis in the figure 3.6), keeping in mind the material isotropy in absence of applied field, we have from equations (3.44) and (3.46),

$$\frac{x^2}{n_o^2} + \frac{y^2}{n_o^2} + \frac{z^2}{n_o^2} + 2r_{41}E_x yz = 1 \tag{3.47}$$

This equation says that in the absence of electric field we have the principal axis along the Cartesian directions chosen, while, in the presence of an electric field we have a change of crystal principal axes. To find the new refractive indices, we must find the directions of new crystal principal axes, or, in others words, we must diagonalize the (3.47). It is easy to show that this happens if we choose the new axes so that [26]

$$\begin{aligned} x &= x' \\ y &= y'\cos\frac{\pi}{4} - z'\sin\frac{\pi}{4} \\ z &= y'\sin\frac{\pi}{4} + z'\cos\frac{\pi}{4}. \end{aligned}$$

In fact, replacing the previous relations in the equation (3.47), we have

$$\frac{x'^2}{n_o^2} + \left(\frac{1}{n_o^2} + r_{41}E_x\right) y'^2 + \left(\frac{1}{n_o^2} - r_{41}E_x\right) z'^2 = 1. \tag{3.48}$$

Therefore, if $n_o^2 r_{41}E_x << 1$, the refractive indices along the new axes (x', y', z') are respectively

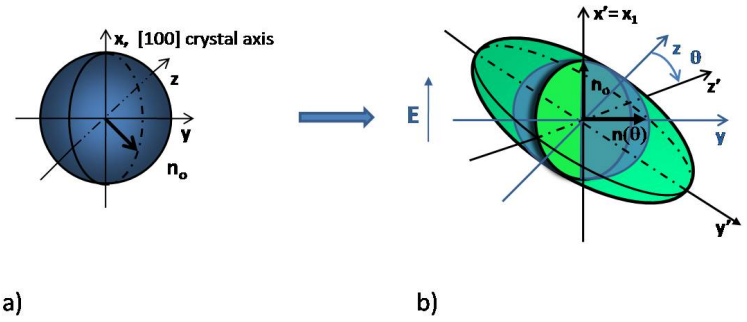

Figure 3.7: Index ellipsoid of a cubic crystal with a $\bar{4}3$ symmetries. **a)** In absence of an electric field the index ellipsoid is a sphere with a ray n_o. **b)** When an external electric field is applied along the [100] crystal axis (the x axis of the reference frame), the ellipsoid z axis is stretched by a quantity $\Delta n = \frac{1}{2} n_o^2 r_{41} E_x$, the ellipsoid y axis is squeezed by a same quantity Δn and the whole ellipsoid rotates by $\frac{\pi}{4}$ around the x *axis*.

$$\begin{aligned} n_{x'} &= n_o \\ n_{y'} &= \frac{n_o}{\sqrt{1 - n_o^2 r_{41} E_x}} \simeq n_o (1 + \frac{1}{2} n_o^2 r_{41} E_x) \\ n_{z'} &= \frac{n_o}{\sqrt{1 + n_o^2 r_{41} E_x}} \simeq n_o (1 - \frac{1}{2} n_o^2 r_{41} E_x). \end{aligned} \tag{3.49}$$

In the case of a cubic crystal with a $\bar{4}3$ symmetries, we can conclude that the electric field $(E_x, 0, 0)$ stretches the ellipsoid index z axis by a quantity $\Delta n = \frac{1}{2} n_o^2 r_{41} E_x$, squeezes its y axis by a same quantity Δn and rotates it by $\frac{\pi}{4}$ around the x *axis*, as shown in figure 3.7.

The refractive index variation for a wave polarized along a direction forming a θ angle respect the y' axis can found by a simple rotation

$$\Delta n\,(\theta) = \frac{1}{2} n_o^3 r_{41} E_x \cos 2\theta. \tag{3.50}$$

In conclusion, if we consider, like in the device which we will shown in the chapter (**??**), a wave propagating along z direction, when an electric field **E** is applied along the x axis (crystal direction [100]) the TE polarization (the polarization along [010] , or, with respect to new axes $[1\bar{1}0]'$) experiences a refractive index

$$n\left(-\frac{\pi}{4}, E\right) = n_o - \frac{1}{2} n_o^3 r_{41} E,$$

while the TM polarization feels the same index felt in absence of the **E** field, that is n_o. The device is, therefore, birefringent.

3.3.2 The quadratic electro-optic effect or Kerr effect

The quadratic electro-optic effect, known as *Kerr effect*, in terms of ellipsoid index coefficients variation is expressed by

$$\Delta\alpha_i = \sum_{l,m=x,y,z} s_{ilm} E_l E_m.$$

The 6×6 tensor s for material with a $\bar{4}3$ symmetries has the form represented in the next expression

$$\begin{bmatrix} \Delta^2\alpha_1 \\ \Delta^2\alpha_2 \\ \Delta^2\alpha_3 \\ \Delta^2\alpha_4 \\ \Delta^2\alpha_5 \\ \Delta^2\alpha_6 \end{bmatrix} = \begin{bmatrix} s_{11} & s_{12} & s_{12} & 0 & 0 & 0 \\ s_{12} & s_{11} & s_{12} & 0 & 0 & 0 \\ s_{12} & s_{12} & s_{11} & 0 & 0 & 0 \\ 0 & 0 & 0 & s_{11}-s_{12} & 0 & 0 \\ 0 & 0 & 0 & 0 & s_{11}-s_{12} & 0 \\ 0 & 0 & 0 & 0 & 0 & s_{11}-s_{12} \end{bmatrix} \begin{bmatrix} E_xE_x \\ E_yE_y \\ E_zE_z \\ E_xE_y \\ E_xE_z \\ E_yE_z \end{bmatrix},$$

so that, if we consider again the case of the previous section, with an applied electric field along the x axes, the non vanish components are only $\Delta\left(\frac{1}{n^2}\right)_1$ and $\Delta\left(\frac{1}{n^2}\right)_2$ and the refraction index variations for TE and TM polarizations of a wave propagating along the z axis, following the same arguments of previous section, are respectively

$$\Delta n_{Kerr}^{TE} = \frac{1}{2} n_o^3 s_{11} E_x \tag{3.51}$$

$$\Delta n_{Kerr}^{TM} = \frac{1}{2} n_o^3 s_{12} E_x. \tag{3.52}$$

3.4 Carrier induced effect

There are three main carrier induced effects on semiconductors refractive index due to electron-electron or hole-hole interactions [46, 47, 48, 49]:

Band-filling effect The number of state in conduction band for an n-type semiconductor is sufficiently low, so that some electrons can fill the band for an appreciable depth. This implies that to optically excite the electrons from the valence band to conduction band, it is required energies greater

than nominal bandgap. As consequence there is an absorption coefficient reduction at energies above the bandgap

$$\Delta\alpha\left(E, N_d\right) = \alpha\left(E, 0\right) - \alpha\left(E, N_d\right)$$

and therefore a refractive index change [**?**], that could be calculated by using Kramers-Kronig transformation :

$$\Delta n_{band-filling} = \Delta n\left(E, N_d\right) = \frac{hc}{2\pi^2}\int_0^\infty \frac{\Delta\alpha\left(E', N_d\right)}{E'^2 - E^2}dE'. \tag{3.53}$$

The same situation subsists for the holes in the p-type semiconductors, but being larger their effective masses, and therefore the density of the states, is smaller the band filling effects.

The injection of electron-hole plasma into semiconductors by electrical or optical means is equivalent to doping effect, since the band filling is the result of free carriers change [49]. The only difference is that the effect is due to both the electrons and the holes. In the case of depletion the sign of $\Delta n_{band-filling}$ is opposite to that injection.

Plasma effect The absorption coefficient can change by *intraband transition* too. In other words, absorbing a photon the electron can move to an higher state within the same band. This phenomena is called *plasma-dispersion effect* and in the Drude model is modelled as being directly proportional to electrons and hole concentrations and to the square of the photon wavelength [49]

$$\Delta n_{plasma} = \left(\frac{e^2\lambda^2}{8\pi^2c^2\varepsilon_o n_o}\right)\left(\frac{N}{m_e} + P\frac{m_{hh}^{1/2} + m_{lh}^{1/2}}{m_{hh}^{3/2} + m_{lh}^{3/2}}\right), \tag{3.54}$$

being e the electron charge, λ the wavelength of incident photon, c the free space light speed, ε_o the vacuum permittivity, n_o the unperturbed material refractive index, m_e the effective electron mass, m_{hh} and m_{lh} the heavy and light holes effective masses, N and P the electron and hole concentrations. The sign of Δn_{plasma} is always negative and its absolute value increases as the photon energy decreases below the bandgap because of the λ^2 dependence.

Experimentally, the relations (3.53) and (3.54) are expressed by means of proportionality constants between the variation of refractive index and the doping level N_d [50] (or free carriers concentrations in the case of injection or depletion):

$$\Delta n_{bf} = \alpha_{bf} N_d \tag{3.55}$$

$$\Delta n_{plasma} = \alpha_{plasma} N_d \tag{3.56}$$

where obviously α_{bf} and α_{plasma} depend on carriers effective masses and photon wavelength. The band filling effect is usually greater than plasma effect, but the latter could be important, depending on carriers type and carriers concentration.

Bandgap Shrinkage When the electrons concentration is large enough, the electron wave functions can overlap, forming a gas of interacting particles. The electrons will repel one another by Coulomb forces and in addition the Pauli principle avoid them to occupy the same state. The net result is a screening of electrons and a decrease in their energy, lowering the energy of conduction band below the bandgap. A similarly effect for the holes increases the maximum of the valence band. The sum of this effects is the bandgap shrinkage [49].

Chapter 4

Single Mode Condition for Rib Waveguide: A New Criterion

Nowadays an increasing number of optical modulators, filters and other functions relevant for telecommunication networks have been proposed [1] [2] [3] [4] [5] [6] [7] as integrated or embedded in dielectric rib/ridge waveguides. Many of them share the common feature of being based on the propagation of the light beam inside a waveguide which has been designed to sustain only its fundamental mode of propagation to allow lower insertion losses when coupled to optical fibers. As observed in [8] most of authors in the past assumed *a priori* that a single-mode rib waveguide must have the same transverse dimensions as a single-mode slab waveguide by attributing it to the Effective Index Method (EIM), so that the rib width would be smaller then the wavelength of the propagating light. But really to this purpose waveguides with large cross section (that is, with lateral dimension and height much greater than the optical wavelength) was usually already employed. Consequently the issue to establish a single mode condition for this waveguide risen and the question is now still open.

To have the first formal studies on the properties of the large cross-section rib waveguide, we have to go back in 1976 with a paper of Klaus Petermann [10], and then in the 1985 in [51]. But only in 1991 Richard A. Soref, Joachim Schmidtchen and Petermann himself [9], performed an Beam Propagation Analysis and given a formula to establish a single mode condition. They tested the formula in the same year [11], using an infrared vidicon camera system to observe a large cross section rib waveguide, realized in Silicon-On-Insulator by means of etching. They observed only

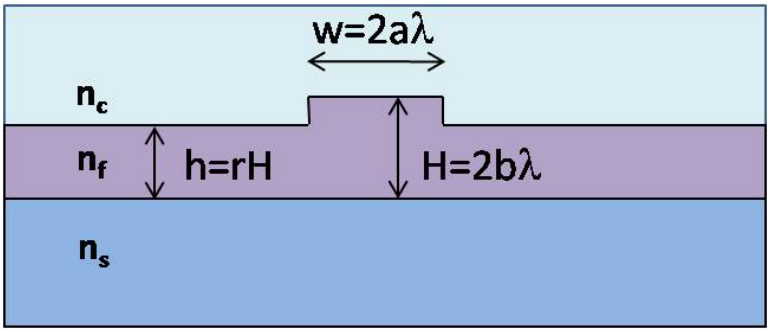

Figure 4.1: Rib waveguide section. H is the rib height; w the rib width; h the slab region height and r the etching complement, i.e. r=h/H.

one vertical mode as predicted by their theoretical analysis.

This formula was considered the right and unequivocal condition for the designer for several years. Nevertheless Pogossian, Vescan and Vosonovici [8], based on the Rickman's experimental data [12] (and concerning this, I have to say that the experimental data available are very few), modified the Soref's formula with an corrective factor.

In the subsequent years the interest about the question is considerable increased. I have found in literature several papers [13, 14, 15, 16] (to cite only someone), which with different methods, semi-analytic, like EIM, Mode Matching or numerical, like Beam Propagation based method, confute or agree either with Soref or with Pogossian or propose correction and new formulas. In these papers other geometry, different from the square, like the trapezoidal (which is the most near to the real case of the etched rib waveguide) are been analyzed too.

After this excursus it seems that there is not an univocal and unambiguous manner to establish if a large cross-section rib waveguide can operate on single mode, so that from this study of the literature, at the begin of my work, I deduced that the first question to solve, to design optoelectronic devices, was to understand which criterion to follow to establish the single mode condition for a large cross-section rib waveguide, or, in others worlds, to found a robust an unambiguously criterion.

In this chapter, after a brief summary about the main and widely used results available in literature, the Soref's formula and the Pogossian's confutation, I expose the new criterion that I find and the comparison with the cited works.

4.1 Main Results on Large Cross-Section Rib Waveguide

The common assumption of all the works about the single-mode condition of the large cross-section rib waveguide is that the height of the ribbed region must be large enough to allow to a slab waveguide with the same height of the guiding film, to support more then the fundamental mode.

Named H the height of the guiding film, being λ the wavelength if the propagating light and, as usually, n_f, n_c and n_s the refractive index if the guiding film, of the cover and substrate, respectively, from the *cut off condition* (2.36) for the slab waveguide, derives that the waveguide is in multi-mode regime if

$$V \equiv \frac{2\pi}{\lambda} H \sqrt{n_f^2 - n_s^2} \geq \arctan \sqrt{\frac{n_s^2 - n_c^2}{n_f^2 - n_s^2}} + m\pi. \tag{4.1}$$

From which, since the (2.39) implies, for $m = 1$,

$$V \geq \pi. \tag{4.2}$$

Rewriting the previous expression in terms of the height normalized to the wavelength, $2b = H/\lambda$ (see figure 4.1):

$$2b\sqrt{n_f^2 - n_s^2} \geq 1, \tag{4.3}$$

we arrives to the starting condition usually used by the authors when studying the single-mode condition for the large cross-section rib waveguide.

4.1.1 The Soref's Condition

Soref and colleagues work is based on the previous Effective Index/Mode Matching analysis performed by Petermann [10], in which some characteristic normalized parameters, related to the geometry structure of the rib waveguide are defined. These parameters are related to the height of the guiding film below the rib, labelled with the index "i" ; with the height of the guiding film outside the rib, labelled with the index "o"; and with the refractive indices n_c, n_f and n_s,

$$w_i = \frac{4\pi b}{q + 4\pi b} \tag{4.4}$$

$$w_o = \frac{4\pi r b}{q + 4\pi r b} \tag{4.5}$$

$$q = \frac{\gamma_c}{\sqrt{n_f^2 - n_c^2}} + \frac{\gamma_s}{\sqrt{n_f^2 - n_s^2}}, \tag{4.6}$$

with $\gamma_{c,s} = 1$ for the HE modes and $\gamma_{c,s} = (n_{c,s}/n_f)^2$ for the EH modes.

Defined an *effective rib parameters*

$$V = \frac{\pi}{2}\frac{a}{b} w_i \sqrt{\delta} \tag{4.7}$$

where is

$$\delta = \left(\frac{w_o}{r w_i}\right)^2 - 1, \tag{4.8}$$

which, like the *V-number* of the slab waveguide, defines the modes cut-off, Petermann found that for each set of rib parameters, there exists a critical value, V_s, such that for

$$V \leq V_s, \tag{4.9}$$

if the complement to the etching, r, satisfies the relation

$$0.5 \leq r \leq 1, \tag{4.10}$$

then the EH_{01}, HE_{01} modes and the higher-order EH_{0m}, HE_{0m} modes cease to propagate.

By plotting V_s as function of δ, Soref and colleagues, derive a boundary between the multi-mode region and the mono-mode region. The boundary is found to be:

$$V_s = \frac{\pi}{2}\left(1 + 0.3\sqrt{\delta}\right). \tag{4.11}$$

Replacing the (4.4), (4.5) and (4.8) in the (4.9), they derives the condition on the aspect ratio a/b (i.e the ratio between the rib normalized width, a, and the rib normalized height, b - see figure 4.1), to have the single-mode regime

$$\frac{a}{b} \leq 0.3 + \frac{r}{\sqrt{1 - r^2}}, \tag{4.12}$$

which, we remind, subsists with the conditions (4.2) and (4.10).

The condition (4.10) is kept in order to assure the vertical cut off of the higher modes. In fact the higher-order mode in the central region will be coupled to the fundamental mode of the lateral slab section, which becomes leaky for $r \geq 0.5$. This happens because for these etching range the effective index of the fundamental slab mode becomes higher than the effective index of any higher-order vertical mode in the central rib region.

To support their thesis, the authors performed an BPM calculation, simulating a propagation of an launched high-order mode by off-axis excitation in a SIO rib waveguide, designed accordantly to the conditions (4.12), (4.10) and (4.3). The analysis results, reported in figure 4.2, shown that in agreement with their prediction, the field intensity is close to the fundamental mode of the rib waveguide. As observed by Reed and Knights, 'Whilst it is not a proof of the concept, it is clearly a demonstration that in this case the hypothesis is reasonable. and that the particularly higher-order modes presented here have leaked away after travelling 2 mm'.

4.1.2 Pogossian's Analysis

Pogossian, Vescan and Vonsovici obseved that, before of the Soref studies, the EIM yields to a simple relation between the transversal sizes of the rib waveguides for the single-mode propagation

$$\frac{a}{b} < \frac{r}{\sqrt{1-r^2}}, \tag{4.13}$$

with the same conditions

$$2b\sqrt{n_f^2 - n_s^2} \geq 1. \tag{4.14}$$

$$0.5 \leq r \leq 1 \tag{4.15}$$

They observed that this formula differs from the Soref'formula by a non negligible factor 0.3. In fact for a fixed value of H and r, the difference in percent is

$$\frac{w_{EIM} - w_S}{w_{EIM}} \geq 0.173,$$

with obvious meaning of the subscript index.

Starting from this observation, they compared the two formulas with the only experimental results available, useful to the aim, the Rickman's data [12]. They plotted the aspect ratio w/H versus the complement to the etching $r = h/H$ extracted from the data. As it is visible in the reported

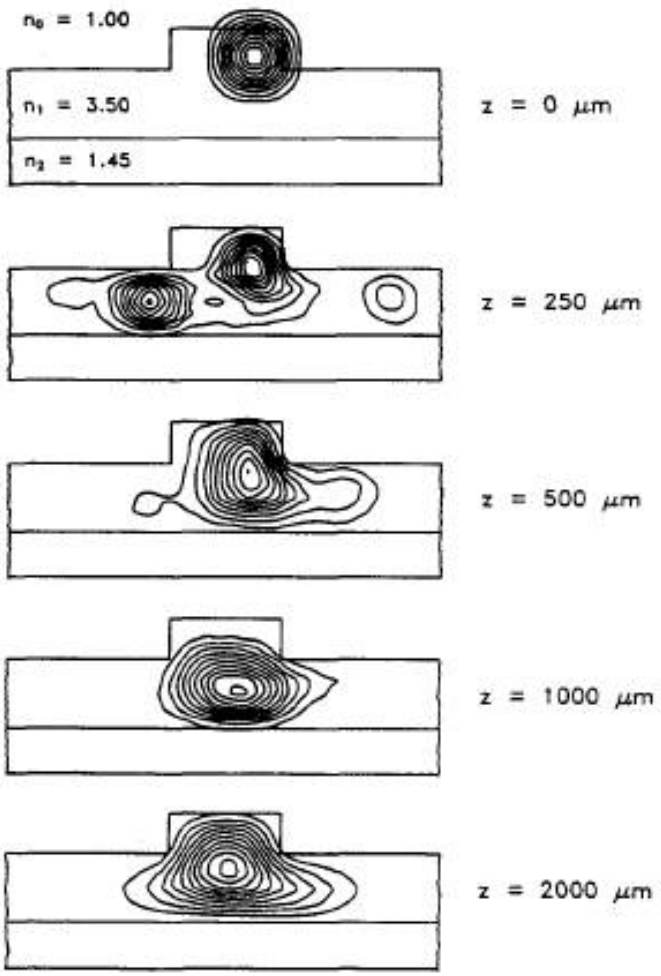

Figure 4.2: Figure extracted by: Soref et al, 'Large single mode RIB waveguides in GeSi-Si and Si-on-SiO2', *Journal of Quantum Electronics*, **27**, pp 1971Ũ1974, 1991.

figure 4.3, the experimental data can be divided into two regions filled either crosses or circles. The zone filled by crosses shows the experimentally verified single-mode propagation region[12]. In the other zone filled by circles the multi-mode guiding condition is satisfied. By fitting the data with the function

$$c + \frac{r}{\sqrt{1-r^2}}, \tag{4.16}$$

they found the value $c = -0.05$, much closer to the value $c = 0$ obtained by EIM than to the Soref's formula. As further experimental evidence of the EIM accuracy, they cited a paper in which a single-mode large cross-section rib waveguide was fabricated using the EIM criterion.

They concluded, therefore, that the EIM offers a stronger and more restrictive condition (compared to the fit results) with an easier physical interpretation.

4.2 Single mode condition: FEM analysis

The problem to establish the single mode condition of a rib waveguide is a eigenvalue problem. Although it is a 2D problem,we have seen in the chapter 2 that it can be reduced to a 2D problem, so that assigned the geometry of the the waveguide section and the refractive index distribution, we have to solve the wave equation for the electric and magnetic field, to determine the supported modes.

Nowadays there are powerful and undiscussed cad tools which allow to solve eigenvalue problem by means of finite elements method. They are consolidated and widely used in a lot of field, the optoelectronics included.

Why we cannot use them?

The answer seems that it cannot possible if we want a general and unambiguous criterion, useful during the devices design, and not a heuristic way to follow every time. We wish to extrapolate a general criterion which, assigned for example the rib height and the height of the lateral region, give us a condition on the aspect ratio w/H in order to have only the propagation of the fundamental mode in the waveguide.

But another issue quiet not negligible becomes visible when solving the Helmholtz equation with numerical techniques: the numerical solver may find solutions that are neither physical nor related to the geometries of the problem, but "inspired" by the boundary conditions. Such solutions are

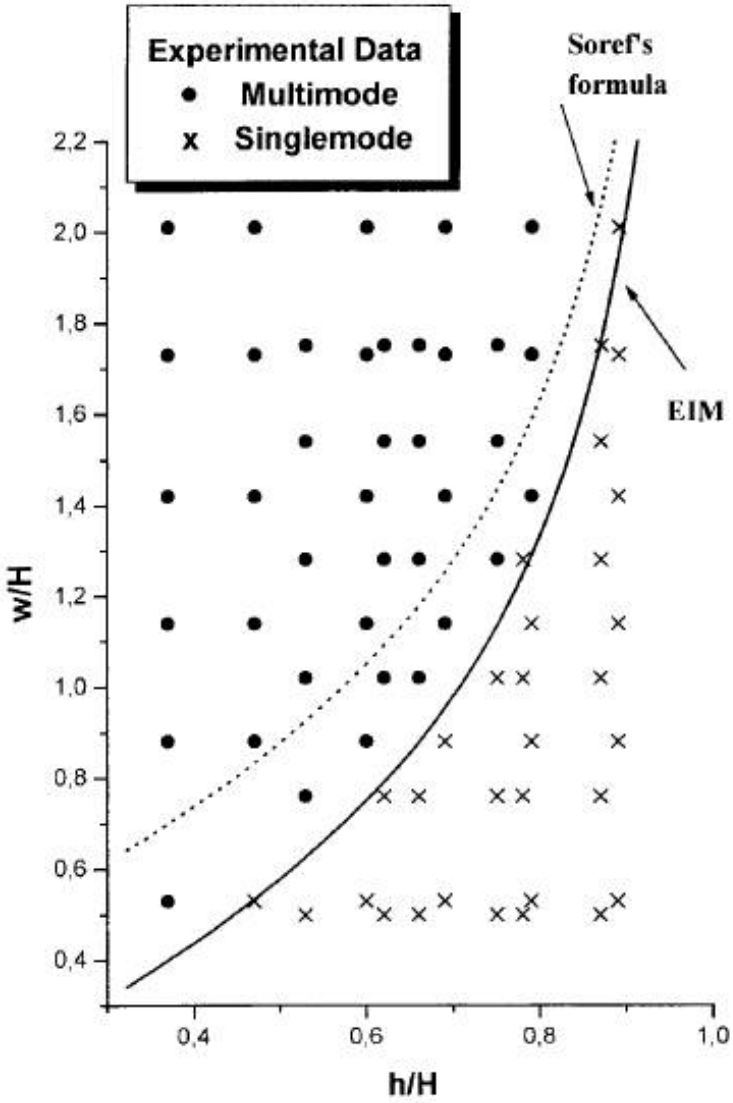

Figure 4.3: Comparison of the single mode condition established by Soref [9] and Pogossian [8] with the experimental data [12]. Figure extracted by Pogossian and al. 'The Single-Mode Condition for Semiconductor Rib Waveguides with Large Cross Section', *Journal of Light Technol.*,**16**,pp 1851-1853, 1998..

usually caused by the unavoidable need to limit the inspection domain to save computational resources.

To be more precise, we note that in the papers before summarized and cited, the lateral dimensions of the waveguide are not considered, but only the width of the rib. This is because the semi-analytical method, like the EIM or the MM, consider the lateral region as ideal slab waveguides, for which the eigenvalues are determined in analytic form. The cross-section of an ideal planar waveguide, as seen in the section 2.3, is extended from infinity to infinity, so that consequently, as derivation the single mode conditions on a rib waveguide are derived for an ideal guide with an infinite cross-section.

Obviously when we work with numerical simulator, we cannot consider real infinite structures. An infinite structure must be simulated by means of suitable boundary conditions. Referring to the figure 4.4, to solve the eigenvalues problem with a FE simulator, we have to impose the following boundary conditions for TE modes:

1. **Dielectric Interfaces** Like in the analytic problem, on the interfaces between the different material 9-14, the boundary conditions must be the continuity condition for the tangent components of the electric field, E, and for the magnetic field, H, and the relative right connection conditions for the normal component (where obviously 'tangent' and 'normal' are referred to the interfaces).

2. **Structures Boundaries** On the boundaries 1-8, to simulate an infinite structure, we have to impose the continuity conditions for the field, expressed in mathematical terms by the Neumann conditions:

$$\widehat{\mathbf{n}} \cdot \nabla \mathbf{u} = 0, \tag{4.17}$$

   where $\widehat{\mathbf{n}}$ is the outward unit normal vector on the boundary and $\mathbf{u}$ is the considered field.

.

Thus, since the solutions result well confined in the vertical direction due to the change of materials above and bottom the guiding film, problems can rise from the lateral boundaries, i.e from the boundaries $1-3$ and $5-7$, in particularly from the boundaries 2 and 6. The imposed boundaries conditions can 'force' the solver to find solutions, when solving the Helmholtz equation, that, as said, are not physical.

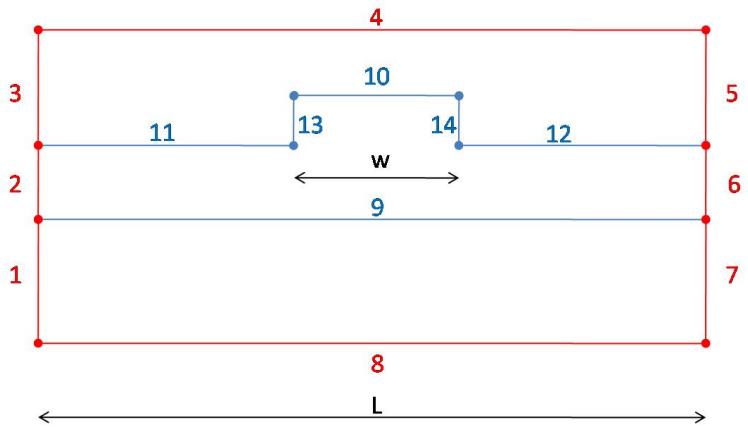

Figure 4.4: Boundaries of a cross-section of a rib waveguide.

Sometimes it can be difficult to distinguish between the physical solution and these 'spurious' solutions. Therefore, if we want to investigate the single-mode condition in rib waveguides, we have to choose a robust criterium to understand whether a numerical solution is either a guided mode or it is leaking away from our guiding structure.

Nevertheless we can draw advantages by this problem.

In fact, the new idea that I have investigated and tested is the following. I suppose the rib waveguide guides modes to be well confined nearby the rib region and thus insensible of the lateral boundaries (referring to the figure 4.4, the boundary 1-3, 5-7); vice-versa I suppose that the non physical solutions have the larger spatial extension and, for this reason, they are more sensible to the lateral boundary conditions. Therefore, by changing the geometrical dimensions of the rib section, I expect an higher difference between the eigenvalue of the first mode solution found with the Dirichlet boundaries conditions (that is vanish field, i.e. $\mathbf{u} = 0$) and the one found with the Neumann boundaries conditions (4.17), when these solutions become without physical meaning (i.e. the mode is no longer guided).

4.2.1 New Criterion

Along this line of argument, I have developed [17] a numerical code based on a general purpose FEM solver, Comsol FEMLAB [] and MATLAB, which, keeping fixed the rib height H, studies the difference $\left|N_{10}^{D} - N_{10}^{N}\right|$ between the effective refractive index of the first higher-order mode found with the

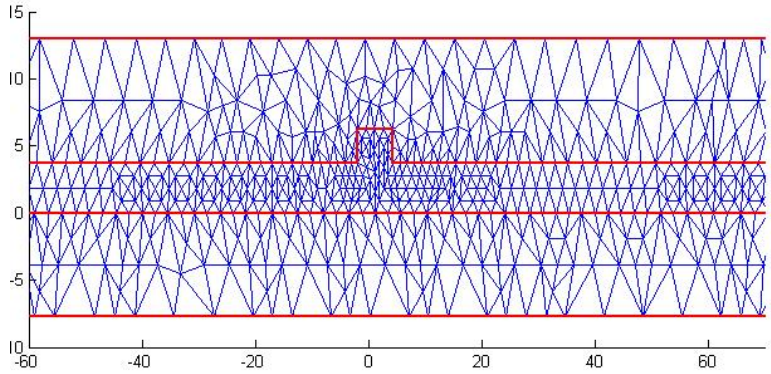

Figure 4.5: Meshgrid generated by the FE simulator (Whiteout refine).

Dirichlet boundaries conditions (N_{10}^D) and the effective refractive index of the first higher order mode found with the Neumann boundaries conditions (N_{10}^N), by changing etching value (i.e. changing the etching complement r, see 4.1) for each width-height ratio value, w/H.

It must be noted that in order to give a meaning to the study, the comparison must be made on the same FE structure, that is on the same geometry and on the same meshgrid. So that I can summarize the first part of the code in this manner:

$$2b\sqrt{n_f^2 - n_s^2} \geq 1. \tag{4.18}$$

1. **Creation of the FE structure**. This means creation of the waveguide section geometry and meshgrid, assigned the materials, that is, the refractive index distribution. This structure is parametric respect to the rib width w, or, better, respect to the normalized width $2a = w/\lambda$ and respect to the rib complement to etching $r = h/H$, while the rib height $H = 2b\lambda$ is kept such that it satisfies the (4.3), that I remind here

2. **Equation Setting up and Boundaries Conditions.** On the FE structure previous made, the Helmholtz equation is set up and the boundaries conditions are imposed: parallely, Dirichlet boundaries conditions and Neumann boundaries conditions are imposed on the lateral boundaries $1-3$ and $5-7$.

3. For each assigned value of the rib width, $w = 2a/\lambda$, the previous problems are solved for the first higher-order mode and the solutions are compared, changing the etching complement vale. In this manner the quantity $\Delta N_{DN}(r) \equiv \left|N_{10}^{D}(r) - N_{10}^{N}(r)\right|$ is estimated.

The typical outcome of this analysis is the plot reported in the figure 4.7, where the quantity $\Delta N_{DN}(r) \equiv \left|N_{10}^{D}(r) - N_{10}^{N}(r)\right|$ is shown. We observe a threshold r*, such that $\Delta N_{DN}(r)$ is essentially negligible for r<r*, while it increases for r>r*, as expected. The r* value is what we expect to be the boundary between a single mode waveguide and a multi-mode one.

In figure 4.7 the comparison between my results, Soref [9] and Pogossian [8] results is shown (to compare the results the analysis was been performed for w chosen between 0.5 and 1.75). As we see, with the chosen threshold, the FEM analysis predicts that the Soref's formula

$$\frac{a}{b} \geq c + \frac{r}{\sqrt{1-r^2}}, \tag{4.19}$$

with $c = 0.3$ (I remind that a and b are the rib half width and the half rib height normalized to the wavelength, respectively, and r is the complement to the etching) is more accurate at lower values of the r parameter, while the Pogossian's approach, which is similar to Soref's formula with c=0, becomes a better approximation when the value of this parameter increases. We must note that Pogossian's results are more conservative because the boundary is always within the single-mode region.

4.3 Discussion

At this point same observations are necessary.

First of all it must be remarked that obviously the hypothesis, according to which the lateral boundaries conditions cannot influence the guided modes, is reasonable if the width L of the numerical domain (see figure 4.4) is chosen large enough. Since, as said, the guided modes are well confined below the rib, the previous condition is satisfied plentifully jet if is $L/2 \geq 10w$. As confirmation of the reasonability of my hypothesis, in the figure 4.8 and 4.9 are shown the results of the FEM analysis for the distribution of the field intensity for the first higher mode, in both the case of Dirichelet and Neumann boundaries conditions for $a/b = 1$ and for several value of r near the threshold, which is estimated to be about 0.54. In particularly the plots

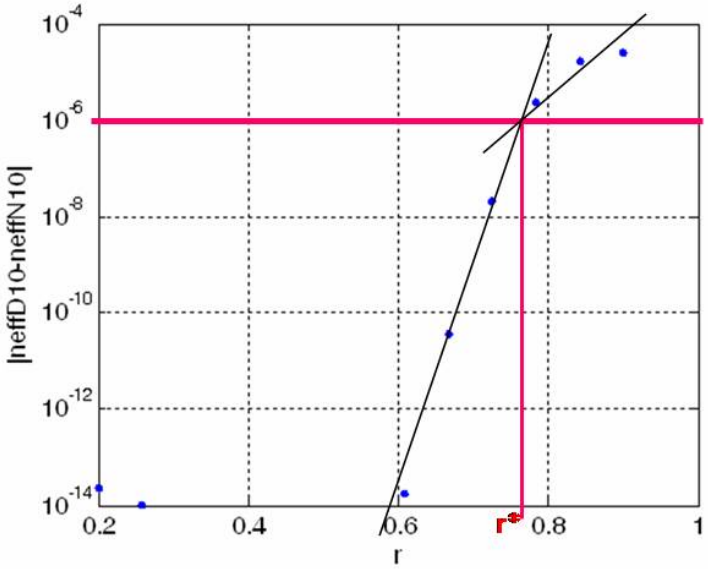

Figure 4.6: Difference between the eigenvalue N_{10}^D of the first mode found with the Dirichlet boundary conditions and the eigenvalue N_{10}^N of the first mode found with the Neumann boundary conditions versus etching rib waveguide complement, r (see figure 4.1). We can observe a threshold, r^* , such that for $r < r^*$ the quantity $\left|N_{10}^D - N_{10}^N\right|$ is essentially negligible, while it increases for $r > r^*$, as expected. The r^* value is what we expect to be the boundary between a singl-mode waveguide and a multi-mode one.

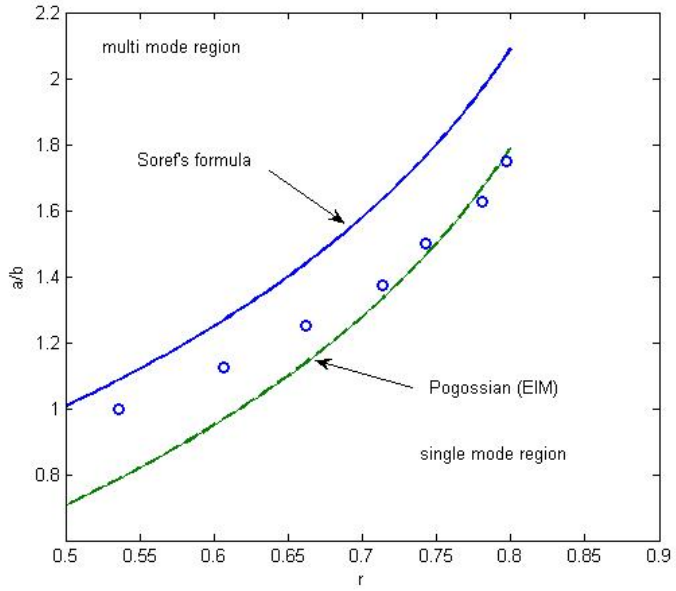

Figure 4.7: Comparison between my FEM analysis results (circle), Soref's formula [9] and Pogossian et al. results [8]. Above the curves is defined the multi-mode region, while below the single mode-region. I have determined the single mode regions by determination of the threshold r* such that the quantity $\left|N_{10}^{D} - N_{10}^{N}\right|$ (that is the difference between the eigenvalue N_{10}^{D} of the first mode found with the Dirichlet boundary conditions and the eigenvalue N_{10}^{N} of the first mode found with the Neumann boundary conditions in the FEM analysis) becomes relevant.

in figure 4.8 are for r<r*, so that, according with my hypothesis, the modes are real guided and well confined near the ribbed region. The plots in figure 4.9 are referred to r>r* and the modes are 'spread' inside the slab region. Obviously from those plots the difference between the two cases are hardly visible, since is $\Delta N \approx 10^{-4}$. It becomes well visible when r increases, as in the second two plots of figure 4.9), where the case $r = 0.9$ is shown even for the fundamental mode with both the boundaries conditions (the two plots in the bottom). As supposed, since the fundamental mode is guided, the FEM analysis solutions are equal with both the boundaries condition and the mode is well confined below the rib. Otherwise for the 10 mode: the solutions in the two cases are different and it is clear the effect of the boundaries conditions, which 'force' the simulator to found solutions that are not physically.

The second observation is about the choice of the threshold r*.

Since the behavior shown in figure 4.6 is repetitive, I have chosen the threshold where a significant change of the slope occurs. Moreover, below that value the quantity ΔN can change enough near the simulator accuracy, while the upper limits seems is unchanged for all the simulations. Therefore this choice it seemed me reasonable.

At least I observe that the criterion is not subject to restriction on r, as the Soref's formula and the Pogossian's one. This means that it can be used for $0 \leq r < 0.5$ too. Moreover even if the presented results are for a rectangular rib waveguide, really there are not restriction on the rib geometry: it can be used with any shape of the ribbed region. Therefore the criterion can be considered a robust criterion.

4.4 Conclusions

In this chapter after an excursus on the literature about the single-mode condition of the rib waveguide and an exposition of the main and widely used results [9] [8], I have shown how Finite Elements Analysis can be used to design single mode optical waveguides. Moreover, after the observation that the necessity to limit the inspection domain, and, therefore, to impose on the lateral boundaries of the waveguide section suitable boundaries conditions, 'forces' the simulator to find solution whiteout physical meaning, but 'inspired' by these boundaries conditions, I have exposed a new criterion based on the discrimination of these 'spurious' solutions of the simulator, supposed

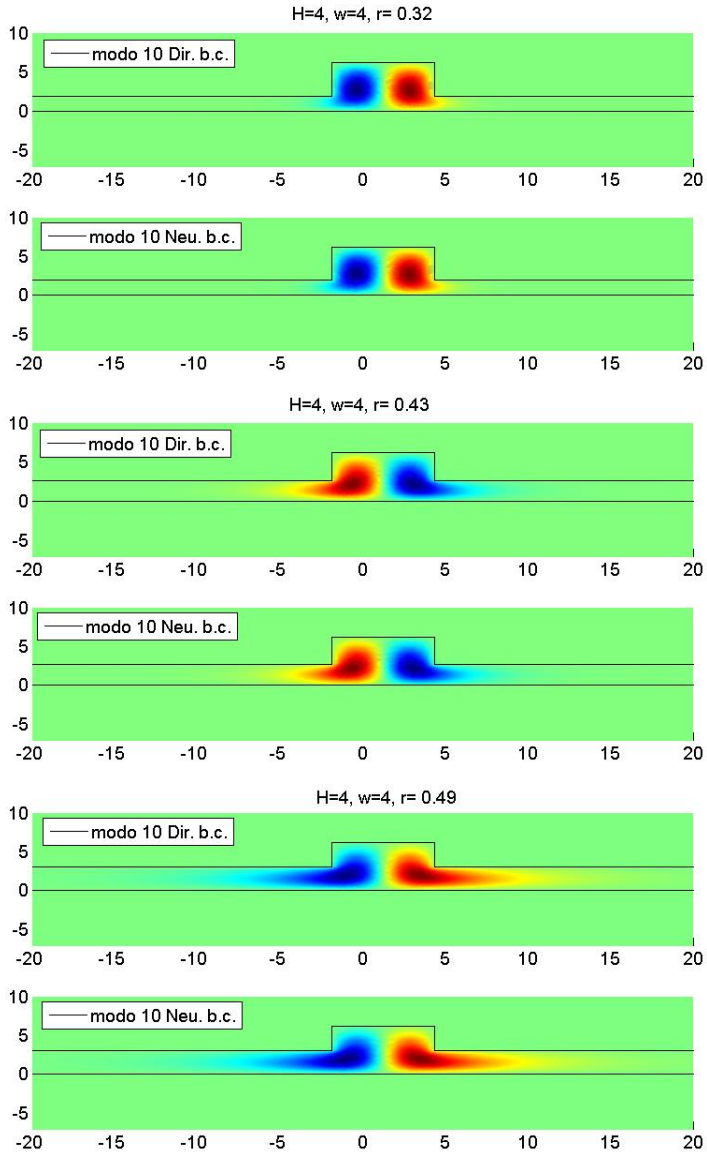

Figure 4.8: Electric field intensity distribution by FEM analysis for the 10 mode of a rib waveguide with $w = H = 4\lambda$ (being λ the field wavelength) and several value of the r<r* in both the case of Dirichelet boundaries conditions and Neumann boundaries conditions. The mode appears well confined near the ribbed region. N.B.: The axes unit are μm and total length of the domain is about $20w$ (the same of figure 4.9). The figure is a particular.

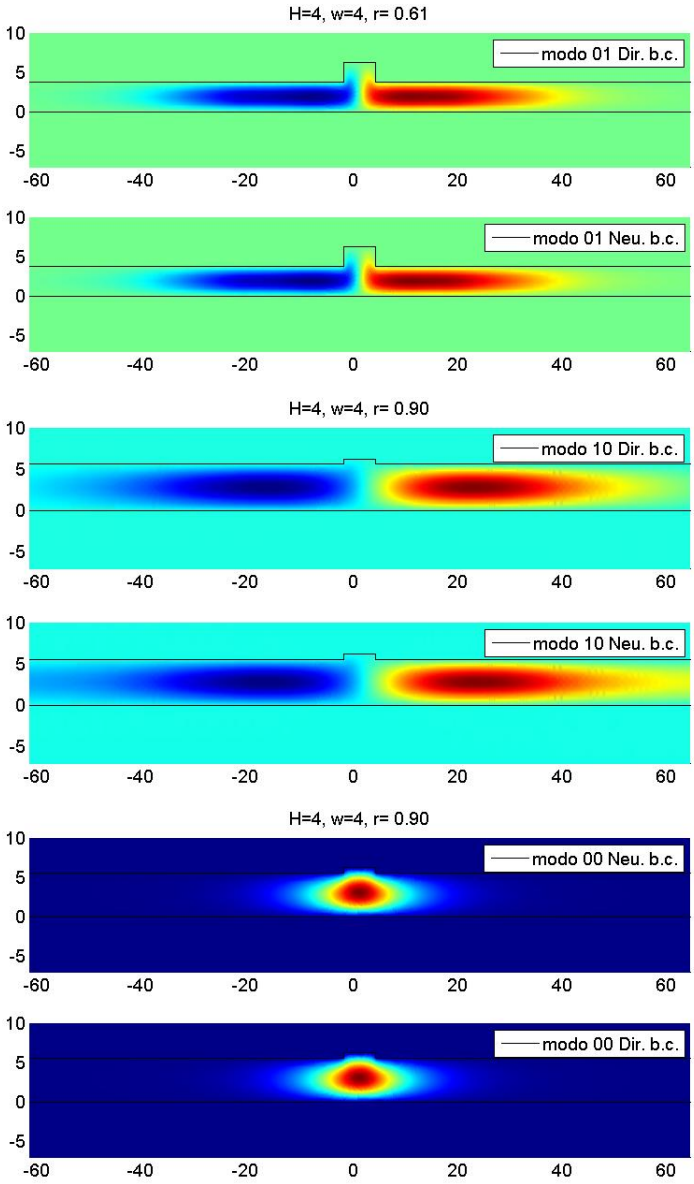

Figure 4.9: Electric field intensity distribution by FEM analysis for a rib with $w = H = 4\lambda$ (being λ the field wavelength) in both the case of Dirichelet boundaries conditions and Neumann boundaries conditions. From top, solutions for the 10 mode with r=0.6; for the mode 10 with r=0.9 and for the fundamental mode with r=0.9. Being r>r* the solutions for the 10 mode appear spread inside the slab region and more sensible to the lateral boundaries, while for the 00 mode the boundaries conditions seem irrelevant, so that seems reasonable the hypothesis that the solutions for the higher mode is 'inspired' by the boundaries conditions and are not physical. N.B.: As in figure 4.8 the axes unit are μm and the total length of the domain is about $20w$.

with a bigger spatial extension inside the slab region, from the physical solution, supposed, beside, well confined near the ribbed region. The criterion establish that, keeping fixed the rib height, there exist a threshold, r*, of the complement to the etching, such that for each value of the rib width, w, the quantity $\left|N_{10}^{D} - N_{10}^{N}\right|$ is essentially negligible for r<r* and thus the corespondent mode really is a physical solution since insensible to the lateral boundaries conditions, while it increases for r>r* and thus the correspondent mode is a spurious solution of the simulator, since it feels the effects of the lateral boundaries conditions. Therefore r* is what we expect to be the boundary between the single-mode regime and the multi-mode one for a rib waveguide.

The criterion is independent from the rib geometry and is not subject to restriction on the etching value. So that it is a robust criterion.

Chapter 5

Totally electrically Induced Bragg Modulator designed by means of new simulation strategy

As said in the introduction of this thesis, due to their high performance in terms of speed and efficiency processing (computing), transmission, and reception of information, the success of the optoelectronic devices in the communication and computational scenery it is increasing, so that parallely, with a view to best design them, it is increasing the necessity to have efficient tools to model and to simulate their behaviors.

This necessity has led in the last year to increase and to promote the development of efficient and comprehensive simulation capabilities for optical devices (both active and passive) including optical, electronic, and thermal processes in a self-consistent fashion, i.e. to integrate an optical package with electronics package to form a self-consistent tool for the optoelectronic integrated circuits.

In fact the old, usual way, to simulate the optoelectronic devices, was to use a multi-dimensional general-purpose electronic devices simulators to obtain the Poisson's equation solution (both carrier continuity and carrier energy balance equation) to have all the electrical and thermal quantity of interest, like potential, carriers distribution, electric field distribution, temperature distribution and so on. Then to solve the scalar wave equations

for the waveguides (that are the most popular basic elements of the opto-electronic integrated devices) by means of a preferred method, that could be numerical or semi-analytic and use numerical or semi-numerical methods to study the light propagation inside the device to predict the optical response.

This method, leaving out of the considerations the designing time, leads to an intrinsic inaccuracy, due to the interpolation of the results when passing from one simulators to an other, or from one method to the others. This source of errors can be critically to predict the very small change of the physical quantity that take place in the optical processes, like the change in the refractive index.

Therefore the first observation is that in the develop of the new tools, it is advisable to use the same method to solve both the Partial Differential Equation (PDE) involved in the electronic/thermal and optical process; and, as second, if the Finite Element (FE) are preferred, the same meshgrid must be used to avoid or minimize the interpolation errors from one grid to the other.

5.1 New Adopted Simulation Strategy

On this new wake, I resort to and improve an in-house code [3], based on a suitable simulation strategy which integrates the capabilities of two of the most popular and consolidate Finite Element simulators, one of electronic devices, as Silvaco/ATLAS, the other a general purpose FE solver, as Comsol Multiphysics, by means of the maybe most powerful and interactive environment in the computational scenery. It is, in fact, a MATLAB® code, which imports the device geometry, the mesh grid and the computed electronic quantity of the interest on this grid (like carriers concentration together the electric field) from ATLAS; defines on the same grid the optical parameters of the material together with their eventually change lows respect the electric parameters (for example, defines the variation of the refractive index due to the application of the external electric field on the grid points); inserts the absorbtion or gain model for a particular structure; furnishes to Comsol Multiphysics the geometry, the grid and all the other said quantities to solve the scalar wave equations in the device and, at least, predicts the optical response (transmittance/reflectance), using the Impedance Matching Matrix Method (see section 3.2).

The code results to be a lot flexible and allows not only, as said, to avoid

the interpolation errors, but to reduce the computational time too.

The better way to explain how the code works is to present a practical example of intensity modulators.

The intensity modulation is reach by means of an modulated phase shift in interferential structures. In the integrated optoelectronics these structures can be the Mach-Zehnder modulator or a multilayer integrated in rib or channel waveguides, and more, as seen, a periodical perturbed waveguides. The phase-shift can be obtained by means of the refractive index change induced by the application of an suitable electric field inside the waveguide, due to the several effects described in the sections 3.3, 3.4. Electrodes on the top of the waveguide and at sides are thus necessary, so that usually the devices section appears as vertical p-i-n junction, inversely polarized to avoid unwanted carriers recombination effects [3] [52] [53] [50] [54].

To predict the response of this kind of devices, assigned the device geometry and known the material parameters (included the *Pockels* and *Kerr tensors*, the *carrier induced effects* coefficients and the refractive index of the materials at the thermal equilibrium) and assigned the device geometry, we have to follow the steps:

1. **Determination of the Electrical Parameters.**
   Determine the carriers concentration and the electric field distribution inside the structure solving the drift diffusion equation and then the Poisson equation, respectively, for each value of the applied reverse bias, i.e. the anode voltage, for the AC analysis and for each value of the time for the Transient analysis.

2. **Determination of the Refractive index change as function of the applied voltage (time)**

   - from the carrier concentration previous determined by means of the empirical formulas 3.55 and 3.56 the refractive index change due to the *carriers effects* as function of the applied anode voltage (time) must be computed;
   - from the determined electric field distribution inside the device section, the contribution of the electrooptic effect must be computed by means of the formulas like the 3.50 and 3.51. These

contributions summed to the carrier induced effects contributions give us the refractive index distribution as function of the applied bias (or time in transient analysis).

3. **Optical characterization** Solve the scalar wave equations for the waveguide to determine the eigenmodes and eigenvalues, that means: determination of the effective refractive index of the supported mode and the field intensity distribution.

4. **Optical Response** Use numerical or semi-numerical methods to study the light propagation inside the device to predict the optical response, that is the device transmittance.

The code fulfils each of the previous steps as follow:

1. Using ATLAS the geometry structure and the meshgrid (Finite Element Method structure), assigned the electrical materials parameters, are made, so that on this meshgrid the carriers distribution and the electric field distribution are determined for each value of the chosen anode voltage applied, V_{an}^k), performing an AC analysis and an transient analysis (responce to an applied anode pulse). So that the out-put are $N(i,j;V_{anode})$ and $E(i,j;V_{an}^k)$, where (i,j) individuates a meshgrid point.

2. The meshing is exported from ATLAS and the refractive index of the materials together with the contributions of the several mentioned effects (EO and CI) are defined on the grid points. So that we have for example, in the case of the band-filling effect and AC analysis:

$$\Delta n_{bf}(i,j;V_{an}^k) = \alpha_{bf} N_d(i,j;V_{an}^k),$$

while for the transient analysis:

$$\Delta n_{bf}(i,j;t_k) = \alpha_{bf} N_d(i,j;t_l),$$

(k is the label which individuates each of the value in the chosen range of the applied anode voltage; while 'l' individuates each of the temporal instants in which we have subdivided the applied voltage impulse)

3. The FEM-structure (geometry and meshgrid) whit the others quantities previous computed on it, are imported in Comsol Multiphysics

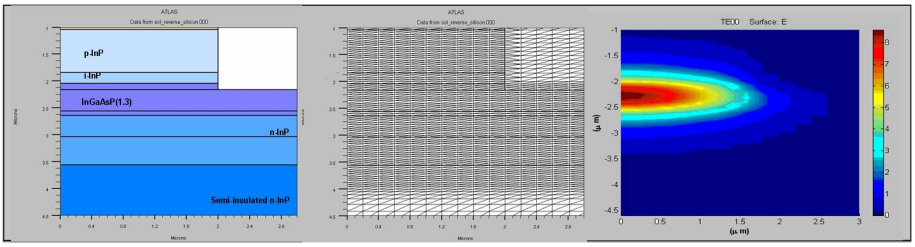

Figure 5.1: From left to right: details of the section structure; corresponding Atlas grid and propagating fundamental TE mode as computed by Comsol Multyphysics FEM simulator

to solve the wave equation. The new out-put is the vector of *effective refractive index* $n_{eff}(V_{an}^k)$ $(n_{eff}(t_l))$

4. At the end the transmittance (equivalently, the reflectance) of the device are computed by means of the Impedance Matching Matrix Method, as described in the section 3.2.

In the next sections we present a device designed by means of the code: an totally electrically induced Bragg Reflector Modulator. We will see how really the very small change of the quantities involved (see figure 5.4) cannot allow errors due to the interpolation on different grid during the design. The crucial point of the adopted simulation strategy, is well visible in the figure 5.1, where, from left to right, are reported the details of the device cross-section (the device is schematically described in the figures 5.2 and 5.3); the corresponding Atlas grid; and the intensity distribution of the propagating fundamental TE mode computed by the Comsol Multyphysics FEM simulator on the same mesh grid.

5.2 Totally electrically induced Bragg Reflector

Using the simulation strategy described in the previous section, we have designed and proposed [] a totally electrically induced Bragg Reflector in InP/InGaAsP materials.

The interest in the possibility to induce a device in an unperturbed waveguide is that it can represent a flexible solution to 'program' on a net of waveguide with same suitable electrodes on the top, same different functions (like intensity modulation, filtering, demultiplexing), or, simply, to choose the light path, driving the applied voltage. In dynamic application, we will

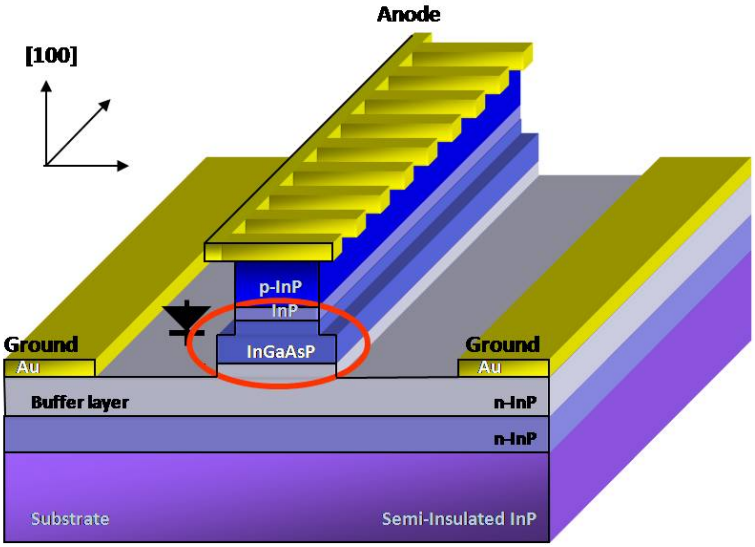

Figure 5.2: Scheme of the proposed induced Bragg Reflector. The section is a vertical InP/InGaAsP p-i-n diode where the InGaAsP region, that is the one with the lower doping, defines the optical channel; while the anode electrode presents a peculiar comb-structure which allows to induce the refractive index periodic perturbation inside the waveguide.

shown as it is possible to realize an intensity modulator, which can reach a theoretical ultra-40 GHz switching speed with a length of 2.5 mm.

5.2.1 Induced Bragg Reflector: description

The main component of the proposed induced devices is shown in the figure 5.2.

We have seen in the sections 3.3 and 3.4 that when a suitable electric field is applied to a semiconductor, different type of effects can induce a refractive index variation depending by field intensity and/or direction. In III-V and particularly in the InP based materials, these effects are all considerable enough to induce a Distributed Bragg Reflector [**?**] in an unperturbed rib-waveguide. Moreover, the attractiveness of the III-V direct-bandgap semiconductor materials, in the optical communication application based on InP, is the possibility to have monolithically integrating optical functionalities with electronic circuitry [**?**] and, in addition, the quaternary (III-V) alloy InGaAsP lattice, matched to InP, offers the possibility to tune the bandgap for different wavelength windows by adjusting its composition.

The device cross-section is a vertical InP/InGaAsP p-i-n diode (see fig-

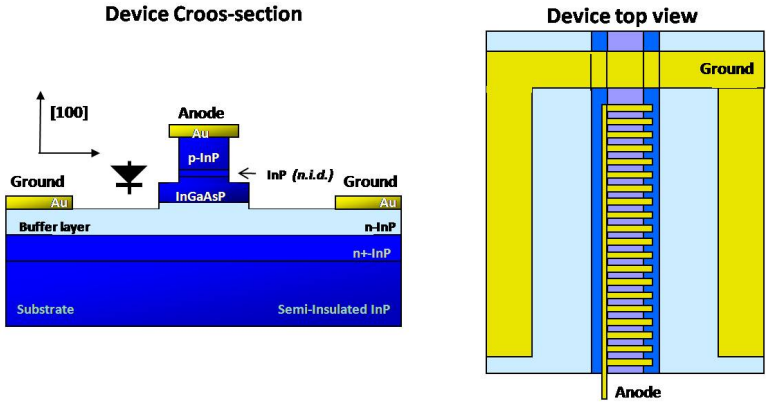

Figure 5.3: Cross-section and top-view if the proposed device. The section is a vertical InP/InGaAsP p-i-n diode where the InGaAsP region, that is the one with the lower doping, defines the optical channel; while the innovative solution is represented by the a peculiar comb-structure of the anode electrode, which allows to induce the refractive index periodic perturbation inside the waveguide.

ure 5.3). We have adopted this cross-section structure from which presented by [3][?] similar to the structure presented in [52]. The n^+-doped substrate serves as possible back contact with other devices on the same substrate; the n-doped InP buffer layer has the function to avoid the attenuation in the substrate and to start in the growing process with a smooth and clean surface. The guiding region is constituted by the InGaAsP layer, which has the refractive index higher then the InP alloy and is a more suitable material for the induced carrier and electrooptic effect [46] [47] [55] [56][49][57]. The thin layer of *non-intentionally-doped* InP between the upper p-InP layer and the guiding layer is used to reduce the very high absorption of p-doped material, thus to have low optical losses [58][59][60][61] [62]. Consequently really the structure appears as an p-i-n-n junctions [50][52]. At least a very thin p^+-InP top layer is present in order to obtain good ohmic contacts with the Au electrode.

The very innovative solutionis is represented by the periodically spaced anode on the top of the waveguide, since, how we will see in the next section, it allows to induce the device in the unperturbed waveguide.

5.2.2 Induced Bragg Reflector: principle of operation

As said, in the InP-based materials the several electric-field based optical effects, which we have described in the chapter 3, take place and none of them can be considered as the dominant one (it is well visible in the graphic of figure 5.4, which shown the contribution of each effect to the refractive index change). Therefore, without biasing the diode the waveguide below the anode electrode is unperturbed and the Bragg reflector is not induced. As consequence the light can travel in the waveguide modulator without being affected by any relevant loss; while, when a negative voltage is applied between anode and cathode, due to the periodic refraction index variation induced in the intrinsic region by the periodically spaced anode, the Bragg mirror is formed along the waveguide.

5.3 An application of the IBR: the induced Bragg Modulator

An application of the *Induced Bragg Reflector* (IBR) is the modulation of the signal intensity by means of voltage pulses on the anode. We will see that, optimizing the Bragg parameters (which in our case are the anode electrode period, his length and the maximum applied reverse voltage) in order to have an as short possible device with an as small possible applied anode voltage, we obtain a 2.5 mm long device, which predicted switching speed is higher than 40 GHz.

5.3.1 Device parameter optimization

In order to optimize the induced Bragg parameters, once determined the the effective refractive index of the fundamental mode (the rib waveguide is designed to work on single-mode) as function of the applied voltage, using the literature value for the electrooptic coefficients and for the carrier induced coefficients reported in the appendix A, the reflectivity spectrum for different electrode period and length was simulated. In figure 5.4 the contribution of each of the effects to the effective refractive index as function of the applied anode voltage and their sum is reported. While in figure 5.5 the reflectivity spectrum for a 2.5 mm long device, optimized to work at 1.55 μm is shown.

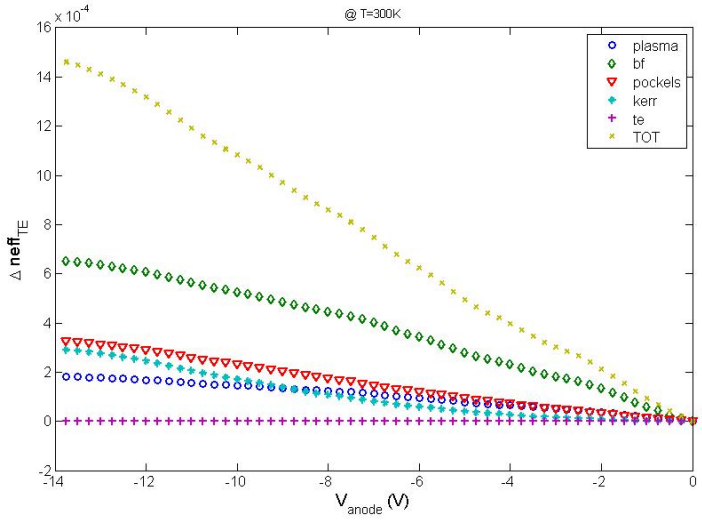

Figure 5.4: Contribution to effective refractive index variation of the several effects induced by the applied anode voltage in the rib waveguide on the top of figure 5.4.

About the period and thus the operating wavelength, we have to note that, since the refractive index of the unperturbed waveguide increase with the voltage, the spectrum shift toward the greater wavelength, as it is possible to see in the figure 5.5. This mens that the period cannot be assigned simply by the *Bragg condition*, which, from the 3.12 results to be

$$\Lambda = \frac{\lambda}{2N_{eff}} \tag{5.1}$$

(where, obviously, N_{eff} is the effective refractive index of the unperturbed waveguide mode), but it must be appropriately chosen.

About the length and the voltage optimization, we must note that there is a twofold approach in the choice of the maximum bias to be applied to the device. It is clear that higher voltages increase the electric field and therefore the phase-shift per unit length. On the other hand as we increase the negative bias we get closer to avalanche breakdown of the junction and consequent injection of free carriers within the optical channel. The other choice is to make the device longer and reduce consequently the applied voltage; in this case we have to tolerate higher propagation losses. By trading off these two constraints we choose a length of 2.5 millim and a maximum bias of -10 V to be applied on the anode.

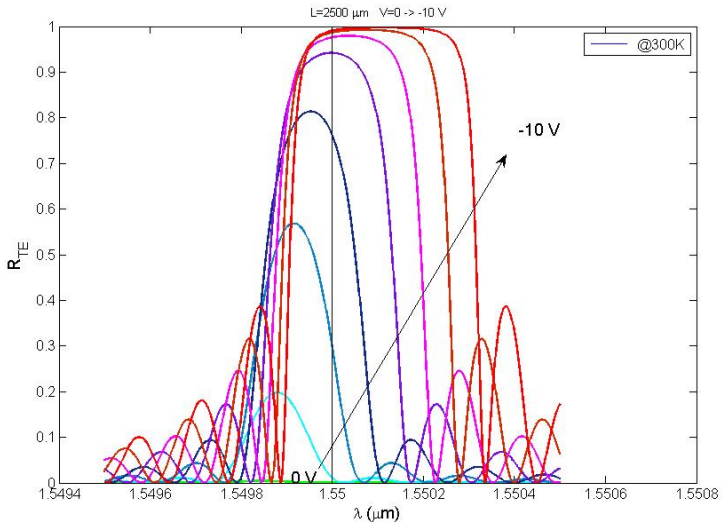

Figure 5.5: Induced Bragg mirror Reflectivity spectrum changing the reverse bias applied between 0 and already. At the chosen operation wavelength of 1.55 µm it changes from 0 to about 1, so that a completely on/off commutation of the light intensity is obtained.

The reflectivity spectrum of figure 5.5, shows as in this case of a 2.5 mm long device, with an electrode period equal to 0.236 µm, increasing the reverse voltage, the light at 1.55 µm is totally reflected by the mirror and an on/off commutation of the light intensity is already obtained between 0 and -10 V.

5.3.2 DC Characteristic

To clarify the DC behavior of this modulator the optoelectronic transfer curve, that is the relationship between reflectivity and applied voltage, for both the TE and the TM polarizations are reported in figure 5.6.

To verify the device stability respect to the temperature, the thermooptic effect has been considered. A temperature change of ± 1 °C has been considered, that is enough for an integrated device. The analysis results are shown in the figure 5.7. We can see that in spite of a little shift of the characteristic, the device behavior it is not compromised.

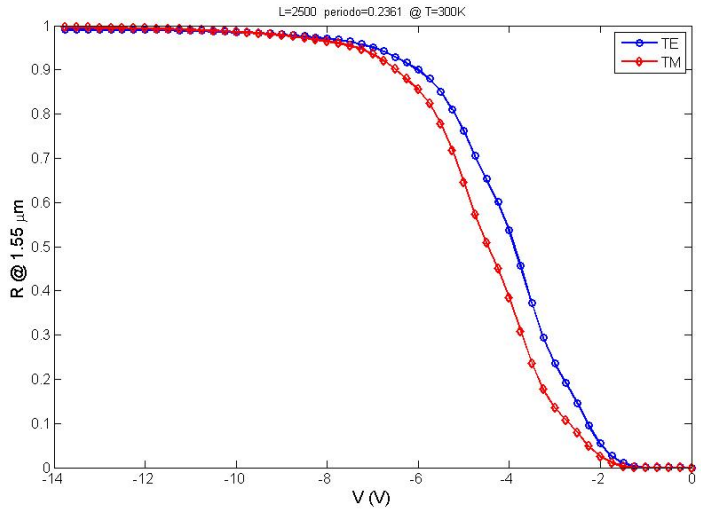

Figure 5.6: Reflectivity at 1.55 µm of the modulator against reverse bias applied for TE and TM polarization.

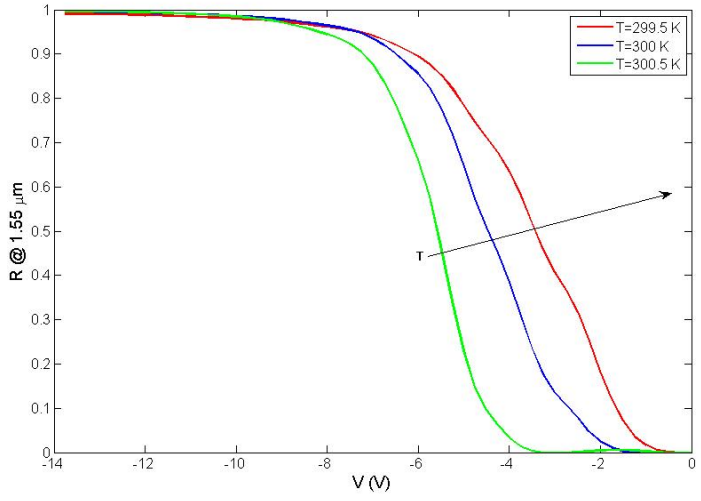

Figure 5.7: Effect of temperature on DC characteristics. On/off modulation is assured between 0 and −10 V.

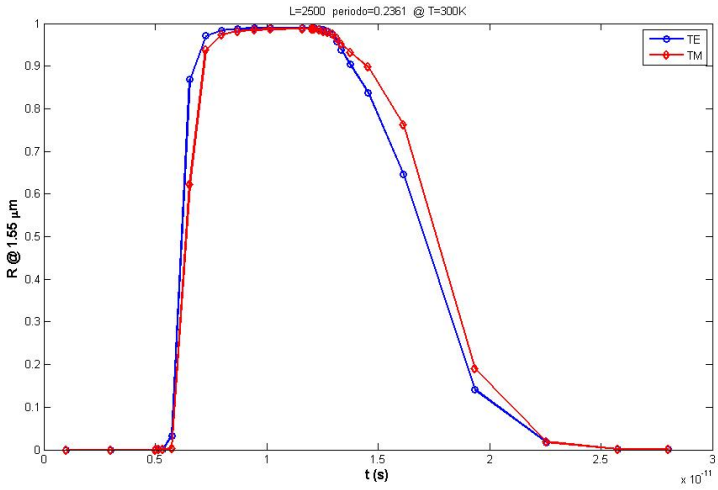

Figure 5.8: Transient behavior of the proposed modulator when driven by a 8 ps long -10 volt square pulse. Rise times estimated of about 2 ps

5.3.3 Transient Analysis

To verify the theoretical switching capability of this device, a negative square voltage pulse has been applied to the anode and reflectivity has been evaluated. The result of this simulation is reported in figure 5.8. We can observe the very fast rise and fall transient (which are of the order of 2 ps and 9 ps respectively) which predict the possible use of this device for ultra 40 Gigabit/s modulation rate. This switching speed is obviously a theoretical upper limit because of the driving amplifiers that have to be impedance matched to the modulator.

5.3.4 Comparison with Mach-Zehnder architecture and other applications

Al least we have compared the transient response of described Induced Bragg Reflector modulator (IBR) to which one of the most popular Mach-Zehnder (MZ) configuration with the same devices section and the same active region length (2.5 mm). The comparison results are shown in figure 5.9. Though the voltage applied for a complete reflectivity on/off switch is lower (3.1 V) for the MZ modulator, the transient response to an 8 ps long pulse is slightly slower. We observe a totally time rise of about 4 ps against 2 ps of Bragg configuration. So, it seems faster the Bragg Modulator, since, moreover, we

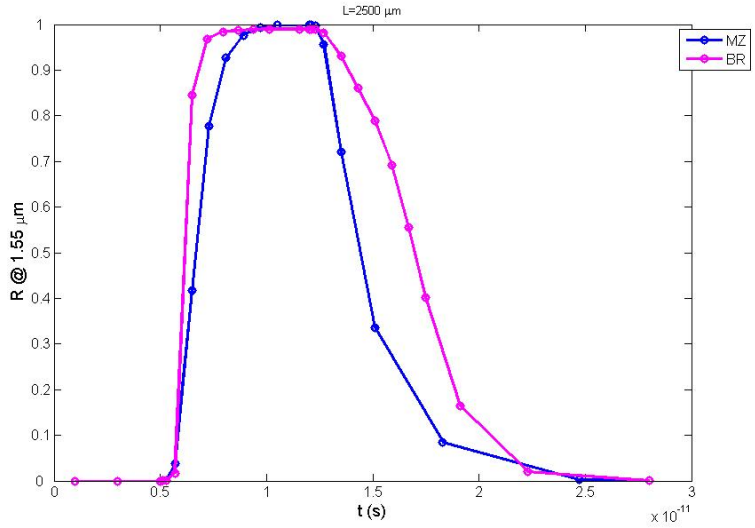

Figure 5.9: Transient response to an 8 ps long −3.1 V pulse of a Mach-Zehnder modulator with the same section and active region length (2.5 mm) of the proposed Bragg modulator. We can observe a rise time longer (about 4 ps)

have to note that to the same length, in the case of the IBR modulator, correspond an half electrode length, i.e. an half capacitance an thus a faster real response. This is true in push-pull configuration of the MZ modulator too, even if in this case the length of the device is half respect the IBM. It is superfluous to note that the area on the chip of a push-pull MZ modulator and of a IBR modulator with the same active region is about the same, since the former is shorter, but double.

Comparing the response of both configuration, shown in the figures 5.8 and 5.10 an other interesting difference appears: while the IBR modulator does not show birefringence, the MZ seems to be birefringent.

To reduce the side-lobes of the Reflectivity Spectra of the grating, apodization [63] could be make, in order to prevent a modulator response increase at low Bias, due to an undesirable shift of the spectra (for example by means of temperature change) or to reduce the device reflection band, if we want a more selective response, for example to have an filter instead of a modulator. In this kind of device obviously the apodization could not be a modulation of the refractive index, but must be realized by mens of modulation or of the

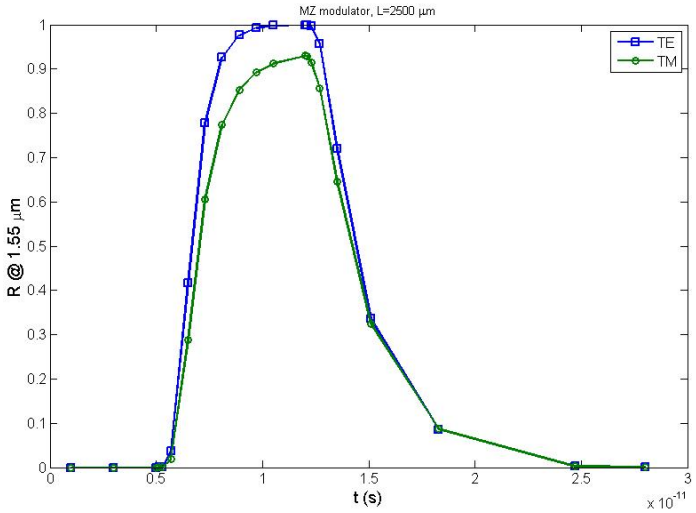

Figure 5.10: Comparison of the transient response to an 8 ps long −3.1 V pulse of a Mach-Zehnder modulator and of the proposed Bragg modulator with the same section and active region length (2.5 mm).

grating period (a good method could be the Randomly Sampled Apodization, RASA, [64]), or by means of the electrode periodicity duty-cycle. The results are the same that in the case of refractive index modulation since what is important is the modulation of the phase shift accumulated in each layer of the grating. Besides both the cited method can be easily realized in the technology process by means of a Focused Ion Beam Deposition, which is a tool usually present during the electronic devices building process [65] as inspection tools, but that could be used to this purpose.

About the technology process, it must be noted that this kind of device do not need etching, implantation or other photolithography steps to write the Bragg reflector, only the metallization step to realize the electrode.

5.4 Conclusion

In this chapter, after the illustration of the adopted simulation strategy for the design of the integrated optoelectronic devices, an integrated modulator in InP/InGaAsP *p-i-n* diode it has been presented. The device is based on the widely used field-effect in the InP derived material, but the peculiarity of our device is the anode electrode comb-structure. It, in fact, allows to induce

the device in an unperturbed waveguide, by means of the applied electric field. The interesting to induce the device in the unperturbed waveguide or net of waveguides is the possibility 'to program', conformity with the necessity, several functions, like wavelength filtering, intensity modulation or, in a fun-configuration demultiplexing, or simply to chose the signal path. In particular we show has an *Induced Bragg Modulator* can potentially reach a transient response greater than 40 GHz, which is perfectly respondent to the actual request of the integrated modulators.

The adopted simulation strategy resorts to the available resources to built a self-consistent tool to design optoelectronic devices. It allows to avoid the inevitable errors of the old strategy due to the use of different tools and methods to predict the device electrical behavior and the optical one, which needed to interpolate the electrical device parameters when imported, for example, from the electric simulator to the optical.

Chapter 6

Conclusions

The main issue which I have faced in this work are the single-mode condition for large cross-section rib waveguide (that is, with lateral dimension and height much greater than the optical wavelength) and the problematic about the simulation strategy of the optoelectronic devices.

The first one could seems a simple and solved question, but although the condition, given by Richard A. Soref, Joachim Schmidtchen, and Klaus Petermann [9], based on previous studies performed by Petermann [10] was widely used, it has been subsequently confuted by several authors, as shown in the chapter 4. The interest on the single-mode condition of the large cross-section rib waveguide lies in the increasing number of devices which have been built as integrated in these waveguide, having a better coupling with the single-mode optical fibers. From the literature it seemed that there was not a unambiguous criterion, but that the condition depend on the device structure and geometry, so that I was induced to face the issue.

I found a new criterion, based on an Finite Element analysis [17], by comparison between the numerical solutions found with Neumann boundary conditions and Dirichlet boundaries conditions applied when solving the eigenvalues problem. The criterion is based on the observation that the necessity to limit the inspection domain, and, therefore, to impose on the lateral boundaries of the waveguide section suitable boundaries conditions, 'forces' the simulator to find solutions without physical meaning, but 'inspired' by these boundaries conditions. These 'spurious' solutions of the simulator are supposed with a bigger spatial extension inside the slab region than the physical solution, which, beside, are supposed well confined near

the ribbed region, so that the first are supposed more sensible to the lateral boundaries conditions than the latest. The criterion establish that, keeping fixed the rib height, there exist a threshold, r*, of the complement to the etching, such that for each value of the rib width, w, the difference between the effective refractive index found for the first higher mode with the Dirichlet boundaries conditions and the effective refractive index found for the first higher mode with the Neumann boundaries conditions, $\left|N_{10}^{D} - N_{10}^{N}\right|$, is essentially negligible for r<r*, so that the corespondent mode is a real physical solution, (since insensible to the lateral boundaries conditions); the said difference increases for r>r*, so that the correspondent mode is a spurious solution of the simulator (since it feels the effects of the lateral boundaries conditions). Therefore r* is what we expect to be the boundary between the single-mode regime and the multi-mode one for a rib waveguide.

The comparison with the Soref's formula shows that the criterion predicts that the Soref's formula is more accurate at lower values of the r parameter, while the Pogossian's analysis (based on the effective Index Methid, [8] and which is similar to Soref's formula except a corrective factor) becomes a better approximation when the value of this parameter increases.

The criterion does not depend on the geometry structure and has not restriction (the Soref's formula and the Pogossian's formula subsist for $0 \leq r < 0.5$). It is thus a robust criteron. Nevertheless it must experimentally confirmed, since the only experimental data which present a sistemtic study on several rib waveguide samples with different etching and width, are not enough dence near the predicted boundary between the single-mode condition and the multi-mode one.

The second issue I faced respond to the request of the last year to develop an efficient and comprehensive simulation capability for optical devices (both active and passive) including optical, electronic, and thermal processes in a self-consistent fashion, i.e. to integrate an optical package with electronics package to form a self-consistent tool for the optoelectronic integrated circuits.

To this purpose, I resort to and improve an in-house code [3], based on a suitable simulation strategy which integrates the capabilities of two of the most popular and consolidate Finite Element simulators, one of electronic devices, as Silvaco/ATLAS, the other a general purpose FE solver, as Comsol Multiphysics, by means of the maybe most powerful and interactive environ-

ment in the computational scenery. It allows to avoid the inevitable errors of the old strategy due to the use of different tools and methods to predict the device electrical behavior and the optical one, which needed to interpolate the electrical device parameters when imported, for example, from the electric simulator to the optical. In fact, since it is based on Finite Element simulators, it uses the same grid to solve both the electrical and the optical equations and to study the propagation conditions.

Tanks to this code I designed an integrated modulator in InP/InGaAsP *p-i-n* diode. The device is based on the widely used field-effect in the InP derived material, but the peculiarity of the device is the anode electrode comb-structure. In fact,it allows to induce the device in an unperturbed waveguide, by means of the applied electric field. What is interesting to induce the device in the unperturbed waveguide or net of waveguides is the possibility 'to program', conformity with the necessity, several functions, like wavelength filtering, intensity modulation or, in a fan-configuration demultiplexing, or simply to chose the signal path. In particular I show has an *Induced Bragg Modulator* can potentially reach a transient response greater than 40 GHz, which is perfectly respondent to the actual request of the integrated modulators.

As future work I hope to realize the device and to test his performance.

Appendix A

InP Optical Properties

The InP belongs to the family of the III-V semiconductors, since it is an alloy between to the Indium (In), belonging to the III-group of the elements table, and the Phosphite (P), belonging to the V-group. As all the others semiconductor, the InP and the quaternary alloys InGaAsP have an energy bandgap, so that they are opaque for light of which the photon energy is higher than the bandgap energy, and transparent for light of which the photon energy is below the bandgap energy.

Their main characteristic and esteem respect to the silicon, which belong to the IV-group of the periodic table, is the direct bandgap against the indirect bandgap, which allows more efficient photon absorbtion and emission processes, since they does not need of the phonon assistance. Moreover as the photon energy is close to their energy bandgap, they show relatively great values of the electrooptic coefficients. All these characteristic allow them to be faster then the Silicon and the Silicon based material, when used as modulators, photo-detectors as well as optical amplifiers.

The InP is a good material for the fabrication of Photonic Integrated Circuits, in which active optical components such as lasers, amplifiers, and optical switches are combined with passive elements such as (de)multiplexers, splitters and couplers on a single chip and moreover, it is suitable for integration of the electrical drive circuitry too, providing very powerful and cost effective solutions for implementing high-speed optical systems.

The possibility to epitaxially grown and to lattice match the ternary and quaternary alloys, InGaAs and InGaAsP, on InP substrate, enlarge the materials potentiality. In fact, by changing the composition of the quaternary alloys, the bandgap wavelength can be tuned anywhere between 0.92 and

1.65 μm, so that tunable active devices like (absorber, laser or amplifiers) and passive function can available in the the telecommunication range, that is the range of lowest losses and lowest dispersion for the optical fibers

A.0.1 InGaAsP on InP: lattice matching condition

The lattice matching condition between the InP substrate and the alloys, depend on latest stechiometry. The used notation for the quaternary alloy composition is $In_{1-x}Ga_xAs_yP_{1-y}$, where is clear that x is the Gallium molar fraction, while y is the Arsenium molar fraction. The lattice condition is given by the following relation between x and y [46][66]

$$x = \frac{0.1896}{04176 - 0.0125y}. \tag{A.1}$$

A.0.2 Energy bandgap

As said, depending on the alloy composition the optical properties change. From the analysis of several alloy champions with different compositon, Nahory *et al.* [66] deduced the following energy bandagap dependence on the composition

$$E_g = 1.35 - 0.72y + 0.32y^2, \tag{A.2}$$

widley used and confirmed in the years [46][49][50][67]. Usually the quaternary alloys are identified by the short noation: $Q(\lambda_g)$, where Q stands for 'quaternary' and λ_g is the absorbtion wavelength, i.e $\lambda_g = hc/E_g$, being h the Planck constant and c the light speed.

A.0.3 Electrooptic and Carrier Induced Effects coefficients

Unfortunately experimentally values for all the effects are not available and often the literature values do not agree. There is a dependence by structure and crystal growth. In the follow we report some of literature values.

- Adachi reports the following values, extracted from his model [46]. For the *electro-optics coefficients* [68]

$$r_{41}^{InP} = 1.41 \times 10^{-12}\ \mathrm{m/V}$$
$$r_{41}^{InGaAsP} = 1.55 \times 10^{-12}\ \mathrm{m/V};$$

  for the quadratic electrooptic coefficients [69]:

$$s_{11}^{InGaAsP} = s_{12}^{InGaAsP} = 4.16 \times 10^{-20}\ \mathrm{m/V^2};$$

while for the *plasma effect*

$$\alpha_{plasma}^{InP} = -4.3 \times 10^{-21}$$
$$\alpha_{plasma}^{InGaAsP} = -5.7 \times 10^{-21}.$$

- Vichant *et al.* [50] use the empirical values reported in [55] and [57] for *electrooptic effect*

$$\begin{aligned} r_{41}^{InP} &= 1.4 \times 10^{-12}\ m/V \\ r_{41}^{InGaAsP} &= 1.55 \times 10^{-12}\ m/V; \end{aligned}$$

while for the Kerr coefficients:

$$s_{11} = s_{12} = 1.5 \times \exp\left(-8.85\Delta E\right) \quad cm^2/V^2;$$

where ΔE is the difference (absolute value), in eV, between the photon energy of guided light and the quaternary material fundamental gap energy. For an photon energy $E_{ph} = 0.8\ eV$ (corresponding to $\lambda_g = 1.55$ μm and a material energy bandgap $E_g^{InP} = 1.35$ eV and $E_g^{InGaAsP} = 0.85$ eV(corresponding to a As molar fraction $y = 0.61$)

$$s^{InP} = 1.15 \times 10^{-17}\ \mathrm{cm}^2/\mathrm{V}^2$$
$$s^{InGaAsP} = 3.79 \times 10^{-17}\ \mathrm{cm}^2/\mathrm{V}^2.$$

From their experimental graphic, we deduce the proportionality constant, for photon wavelength of 1.55 μm (E_g=0.8 eV):

$$\alpha_{bf}^{InP} \approx -5 \times 10^{-21}$$
$$\alpha_{bf}^{InGaAsP} \approx -30 \times 10^{-21}$$

- In his PhD dissertation, Maat from the available model develop same theoretical curves which give the refractive index change as function of the photon wavelength and parameterized respect to the quaternary alloy composition.

  He models the linear electrooptic effect with the Adachi model and then uses the modified single-oscillator model of Fiedler and Schlachetzki [48] for the calculation of the composition dependent refractive index change of InP/InGaAsP. Successively, experimentally he determines an

increment factor for the Pockels coefficient of 1.07, so that his value for Pockels coefficients are:

$$r_{41}^{InP} = 1.35 \times 10^{-12} \text{ m/V}$$
$$r_{41}^{InGaAsP} = 1.65 \times 10^{-12} \text{ m/V}.$$

For the quadratic electrooptic effect, he uses the Faist [54] theoretical values, experimentally confirmed by Krähenbühl [70], then the Fiedler and Schlachetzki model to derive again the composition dependence:

$$s_{11}^{InP} \sim 1.5 \times 10^{-20} \text{ m}^2/\text{V}^2$$
$$s_{12}^{InP} \sim 1 \times 10^{-20} \text{ cm}^2/\text{V}^2,$$

$$s_{11}^{InGaAsP} = 1.19 \times 10^{-19} \text{ cm}^2/\text{V}^2$$
$$s_{12}^{InGaAsP} = 2.15 \times 10^{-19} \text{ cm}^2/\text{V}^2,$$

He uses the Bennet model [49] to model the refractive index change due to the *band filling effect* as function of the doping level; then he uses the modified single-oscillator model [48] for the calculation of the composition dependent refractive index change of InP/InGaAsP. From his graphics, we deduce, considering a $Q()$ InGaAsP:

$$\begin{aligned} \alpha_{bf}^{InP} &\approx -3 \times 10^{-21} \\ \alpha_{bf}^{InGaAsP} &\approx -20 \times 10^{-21} \end{aligned}$$

while for the *plasma* effect his calculation are in agreement with Adachi. In fact results:

$$\begin{aligned} \alpha_{plasma}^{InP} &\sim -4 \times 10^{-21} \\ \alpha_{plasma}^{InGaAsP} &\sim -5 \times 10^{-21}. \end{aligned}$$

List of Figures

Bibliography

[1] G. Breglio, G. Coppola, A. Cutolo, A. Irace, M. Bellucci and M. Iodice, "Temperature Optical Sensor Based on a Silicon Bi-Modal Y Branch," in *Silicon-based and Hybrid Optoelectronics III* (David J. Robbins, John A. Trezza, Ghassan E. Jabbour, ed.), vol. 4293, pp. 155–161, SPIE, May 2001.

[2] A. Irace, G. Breglio and A. Cutolo, "All Silicon optoelectronic modulator with 1 GHz switching capability," *Electronics Letters*, vol. 2, pp. 232–233, January 2003.

[3] F. M. De Paola, V. d'Alessandro, A. Irace, J. H. den Besten, and M. K. Smit, "Novel optoelectronic simulation strategy of an ultra-fast InP/InGaAsP modulator," vol. 256, pp. 326–332, 2005.

[4] R. Jones, A. Liu, H. Rong, M. Paniccia, O. Cohen and D. Hak, "Lossless optical modulation in a silicon waveguide using stimulated Raman scattering," *Optics Express*, vol. 13, p. 1716, March 2005.

[5] I. Kiyat, A. Aydinli and N. Dagli, "High-Q silicon-on-insulator optical rib waveguide racetrack resonators," *Optics Express*, vol. 13, pp. 1900–1905, March 2005.

[6] D. Y. Wanga, K. P. Lorb, K. K. Chungb, H. P. Chanb, K. S. Chiangb, H. L. W. Chana and C. L. Choy, "Optical rib waveguide based on epitaxial Ba0.7Sr0.3TiO3 thin film grown on MgO ," *Thin Solid Films*, vol. 1-2, pp. 329–333, July 2006.

[7] Y. Zhang , T. M. Benson1, P. Sewell, A. Vukovic1, D. Zhang1, W. J. Pan, A Loni, D. Furniss and A. B. Seddon, "The Design of Single Mode Large Cross-section Glass-based Waveguides for Photonic Integrated Circuits," *Optical and Quantum Electronics*, vol. 38, pp. 97–110, April 2005.

[8] S. P. Pogossian, L.Vescan and A. Vonsovici, "The Single-Mode Condition for Semiconductor Rib Waveguides with Large Cross Section," *Journal of Lightwave Technology*, vol. 16, pp. 1851–1853, 1998.

[9] R. A. Soref, J. Schmidtchen, and K. Petermann, "Large single mode RIB waveguides in GeSi-Si and Si-on-SiO2," *Journal of Quantum Electronics*, vol. 27, p. 1971Ű1974, August 1991.

[10] K. Petermann, "Properties of optical RIB waveguides with large cross section," *Archiv flur Electronik und Ubertragungstechnik*, vol. AEU-30, p. 139Ű140, 1976.

[11] J. Schmidtchen, A. Splet't, B. Schuppert, K. Petermann and G. Burbach, "Low Loss Single-Mose Optical Waveguide with Large Coss-Section in Silicon-On-Insulator," *Electronics Letters*, vol. 27, pp. 1486–1487, Augusst 1991.

[12] A. G. Rickman, G. T. Reed, and F. Namavar, "Silicon-on-insulator optical RIB waveguide loss and mode characteristics," *Journal of Lightwave Technology*, vol. 12, p. 1771Ű1776, October 1994.

[13] J. Lousteau, D. Furniss, A. B. Seddon, T. M. Benson, Senior Member, A. Vukovic, and P. Sewell,, "The Single-Mode Condition for Silicon-on-Insulator Optical Rib Waveguides With Large Cross Section," *Journal of Lightwave Technology AUGUST 2004*, vol. 22, no. 8, pp. 1923–1929, 2004.

[14] O. Powell, "Single-Mode Condition for Silicon Rib Waveguides," *Journal of Lightwave Technology*, vol. 28, pp. 1851–1855, 2002.

[15] J. Xia and J. Yu, "Single-mode condition for silicon rib waveguides with trapezoidal cross-section ," *Optics Communications*, vol. 230, pp. 253–257, February 2004.

[16] X. Xing, X. Deng and B. Li, "Analysis of GaN-based single-mode rib waveguide with large cross section," *Journal of Microlithography, Microfabrication, and Microsystems*, vol. 5, p. 33009, July 2006.

[17] M. De Laurentis, A. Irace and G. Breglio, "Determination of single mode condition in dielectric rib waveguide with large cross section by finite element analysis ," *Optical and Quantum Electronics*, vol. 6, no. 1-3, 2007.

[18] Integrated Systems Engineering, Zurich, Switzerland, www.ise.ch, *DESSIS*.

[19] Synopsys, CA, USA, www.synopsys.com, *Taurus-Medici*.

[20] Silvaco Data Systems, www.silvaco.com, *ATLAS*.

[21] Institute for Microelectronics, TU Vienna, Austria,, www.iue.tuwien.ac.at, *Minimos-NT*.

[22] Silvaco Data Systems, www.silvaco.com, *VCSEL Vertical Cavity Surface Emitting Laser Simulations*.

[23] Crosslight Software Inc., www.crosslight.com, *Crosslight Device Simulation software informationsInc*.

[24] E. Marcatili, "Dielectric rectangular waveguides and directional coupler for integrat," *Bell System Techinical Journal*, vol. 48, pp. 2071–2102, 1969.

[25] K. Chiang, "Dual Effective-Index Method for the Analysis of Rectangular Waveguides," *Applied Optics*, vol. 25, pp. 2169–2174, 1986.

[26] Amnon Yariv, *Quantum Electronic*. J. Wiley and Sons, 3 ed., 1987.

[27] M. Born and E. Wolf, *Principles of Optics*. Cmbridge University Press.

[28] S. Wang, "Proposal of periodic layered waveguide structures for distributed lasers," *Journal of Applied Physics*, vol. 44, pp. 767–780, 1973.

[29] A. Basu and J. M. Ballantyne, "Random fluctuations in first order waveguide grating filters," *Applied Optics*, vol. 18, pp. 2575–2579, 1979.

[30] G. Bjork and . Nilsson, " new exact and efficient numerical matrix theory of complicated laser structures: properties of asymmetric phase-shifted DFB lasers," *Journal of Lightwave Technology*, vol. LT-5, pp. 140–146, 1987.

[31] R. T. P. Verly and J. Lit, "Application of the effective index method to study of distributed feedback in corrugated waveguides. TE polarization," *Journal of Optical Society of America*, vol. 70, pp. 964–968, 1980.

[32] R. T. P. Verly and J. Lit, "Application of the effective index method to study of distributed feedback in corrugated waveguides. TM polarization," *Journal of Optical Society of America*, vol. 70, pp. 1218–1221, 1980.

[33] K. A. Winick, "Effective index method and coupled-mode theory for almost periodic waveguide gratings: a comparison," *Applied Optics*, vol. 31, pp. 757–764, August 1992.

[34] P. H. L. Khun, M.L. Dakss and B. Scott, "Deflection of optical guided waves by a surface custic wave," *Applied Physics Letters*, vol. 17, p. 265, 1970.

[35] R. Dixon, "The photoelastic properties of selectd materials and their releance to acustic light modulators and scanner," *Jornal of Applied Physics*, vol. 38, no. 4, 1967.

[36] A. Yariv and M. Nakamura, "Periodic structures for Integrated Optics," *Journal of Quantum Electrnics*, vol. 13, pp. 233–253, April 1977.

[37] a. R. D. B. William Streifer, Donald R. Scifres, "Coupling Coefficients for Distributed Feedback Single- and Double-Heterostructure Diode Lasers," *Journal of Quantum Electronics*, vol. QE-11, 1975.

[38] H. Kogelnik and C. V. Shank, "Coupled mode theory of distributed feedback lasers," *Journal of Applied Physics*, vol. 43, pp. 2327–2335, May 1972.

[39] A. Yariv and M. Nakamura, "Coupled-Mode theory for guided-wave optics," *Journal of Quantum Electrnics*, vol. QE-9, 1973.

[40] R. D. B. William Streifer and D. R. Scifres, "Coupling coefficients and propagation constants in guided wave distributed feedback lasers," *Journal of Applied Physics*, vol. 46, pp. 946–948, 1975.

[41] S. P. K. Handa and T. Tamir, "Improved perturbation analysis of dielectric gratings," *Applied Physics*, vol. 5, 1975.

[42] L. Poladian, "Couled-mode theory for light propagating hrough deep nonlinear grating," *Physical Review E*, vol. 48, 1993.

[43] L. P. J.E. Sipe and C. de Sterke, "Propagation through nonuniform grating," *Journal of Optical Society of America A*, vol. 11, 1994.

[44] C.Martijn de Sterke, D. Salinas and J.E. Sipe, "Couled-mode theory for light propagating hrough deep nonlinear grating," *Physical Review E*, vol. 54, 1996.

[45] G. Coppola, *Analysis and Design of Bragg Grating based optoelectronic devices*. PhD thesis, Università degli Studi di Napoli Federico II, Napoli, Italy, 2001.

[46] S. Adachi, "Materials parameters of ingaasp and related binaries," *Journal of Applied Physics*, vol. 53, p. 8775, 1982.

[47] S. Adachi, *Physical properties of III-V semiconductor compound*. New York: Wiley & Sons, 1992.

[48] F. Fiedler and A. Schlachetzk, "Optical parameters of inp-based waveguides," *Solid State Electron.*, vol. 30, p. 73, 1987.

[49] B. Bennet, "Carrier-induced change in refractive index of inp, gaas and ingaasp," *IEEE Journal of Quantum Electronics*, vol. 26, p. 116.

[50] J. V. et al., "Inp/gainasp guided-wave phase modulators based on carrier-induced effects: Theory and experiment," *Journal of Lightwave Technology*, vol. 10, p. 63, 1992.

[51] N. Dagli and C. G. Fonstad, "Analysis of rib dielectric waveguides," *Journal of Quntum Electronics*, vol. 21, pp. 315–321, 1985.

[52] T. Uitterdijk, *Integrated Electro-Optical switches on InP*. PhD thesis, DIMES, Delft, The Netherlands, 1997.

[53] K. Vreeburg, *InP-besed Photonic Integrated Circuits for Wavelenght Routing and Switching*. PhD thesis, DIMES, Delft, The Netherlands, 1997.

[54] J. Faist and F. Reinhart, "Phase modulation in gaas/algaas double heterostructures. i theory," *Journal of Applied Physics*, vol. 87, p. 6989.

[55] P. Albrecht, *Integrated Optics*. 1983.

[56] H. Bach, "Electro-optical light modulation in ingaasp/inp double heterostructure diodes," *Appl. Phys. Lett*, vol. 42, p. 692, 1983.

[57] C. Bornholdt in *Proc. 3rd Eur, Conf. on Integrated Optics (ECIO'85)*, (Berlin), 1985.

[58] Y. T. E. A. H. Inoue, T. Kato and K. Ishida, "Inp-based optical switch module operating through carrier-induced refractive index change," *Optical Engineering*, vol. 29, pp. 191–199, 1990.

[59] M. M. F. Ito and T. Tanifuji, "A carrier injection type optical switch in gaas using free carrier plasma dispersion with wavelength range from 1.06 to 1.55 pm," *Journal of Quantum Electronics*, vol. 25, pp. 1677–1681, 1989.

[60] F. Ito and T. Tanifuji, "Carrier-injection-type optical switch in gaas with a 1.06-1.55 iim wavelength range," *Applied Physics Letters*, vol. 54, pp. 134–136, 1989.

[61] H. M. T. K. K. Ishida, H. Nakamura and H. Inoue, "Inp/gainasp guided-wave phase modulators based on carrier-induced effects: Theory and experiment," *Applied Physics Letters*, vol. 50, pp. 141–142, 1987.

[62] G. S.-R. G. Muller, L. Stoll and U. Wolf, "Low current plasma effect optical switch on inp," *Electronics Letters*, vol. 26, pp. 115–117, 1990.

[63] T. Erdogan, "Fiber Grating Spectra," *Journal of Lightwave Technology*, vol. 15, p. 1277, August 1997.

[64] M. Tormen, S. Ghidini, P. Crespi, D. Chacon, A. Nottola, S. Sardo, D. Crippa, M. Di Muri, G. Zuliani and F. Giacometti, "Randomly Sampled Apodization in Bragg Gratings," *Journal of Lightwave Technology*, vol. 24, no. 4, pp. 946–948, 2006.

[65] Steve Reyntjens and Robert Puers, "A review of focused ion beam applications in microsystem technology," *Journal of Micromechanics and Microengineering*, vol. 11, p. 287Ű300, 2001.

[66] R.E. Nahory, M. A. Pollack, W. D. Johnston Jr. and R. L. Bsrns, "Band gap versus composition and demonstration of vegard's law for ingaasp lattice matched to inp," *Applied Physics Letters*, vol. 33, p. 659, 1978.

[67] P. Maat, *InP based integrated MZI switches for optical communications.* PhD thesis, University of Delft, Delft, The Netherlands, 1992.

[68] S. Adachi and K. Oe, "Linear electroptic effect in zincblende type semiconductors: Key proprerties of ingaasp relevant to devices design," *Journal of Applied Physics*, vol. 56, pp. 74–80, 1984.

[69] S. Adachi and K. Oe, "Quadratic electroptic effect (kerr) in zincblende type semiconductors: Key proprerties of ingaasp relevant to devices design," *Journal of Applied Physics*, vol. 56, pp. 1499–1504, 1984.

[70] R. Krähenbühl, *Electro-Optic Space Switches in InGaAsP/InP for Optical Communication*. Konstanz, Hartung-Gorre, 1998.

List of Publications

1. G. Mauro D'Ariano, Martina De Laurentis, Matteo G. A. Paris, Alberto Porzio and Salvatore Solimeno, *Quantum Tomography as a Tool for the Characterization of Optical Devices*, J. Opt. B 4, S127ŰS132 (2002);

2. A. Porzio, P. Aniello, A. Chiummo, V. D'Auria, M. De Laurentis, S. Solimeno and M. G. A. Paris *A novel quantum cryptographic scheme based on bright twin beams*, Proceedings of the 8th International Conference on Squeezed States and Uncertainty Relations, Rinton Press (2003), 328-335;

3. V. D'Auria, A. Chiummo, M. De Laurentis, A. Porzio, S. Solimeno, M. G. A. Paris. *Tomographic characterization of OPO sources close to threshold* , Optics Express, vol 13, 948-956 (2005);

4. M. De Laurentis, A. Irace, and G. Breglio, *Determination of single mode condition in dielectric rib waveguide with large cross section by finite element analysis*, J. Comput. Electronics, (2006).

5. M. De Laurentis, A. Irace, and G.Breglio, *Finite element analysis of the single mode condition in dielectric rib waveguides with large cross section*, Proc. AISEM, (2006).

6. M. De Laurentis, A. Irace and G.Breglio, *Determination of single mode condition in dielectric rib waveguides with large cross section by finite element analysis*, Proc. IWCE, May 2006.

7. M. De Laurentis, F. M. De Paola, V. d'Alessandro, A. Irace and G. Breglio, *InP/InGaAsP electrically controlled Bragg modulator for over 40-Gbit/s modulation speed*, Proc. SPIE, vol. 6350, 63500E, Jun. 2006,

presented at Workshop on Photonic Components for Broadband Communication.

8. M. De Laurentis, F. M. De Paola, V. d'Alessandro, A. Irace, and G. Breglio, *Electrically induced Bragg modulator for ultrafast light modulation in Indium Phosphide devices*, Proc. IEEE 6th International Conference on NUmerical Simulation of Optoelectronic Devices (NUSOD), pp.121-122, Sep. 2006.

9. A. Irace, M. De Laurentis, V. dŠAlessandro, F. M. De Paola and G. Breglio, *An ultrafast InP/InGaAsP optical modulator*, SPIE newsroom, 2006.